JARO 18: 301–322 (2017)
DOI: 10.1007/s10162-016-0605-5

JARO
Journal of the Association for Research in Otolaryngology

Research Article

Predictions of the Contribution of HCN Half-Maximal Activation Potential Heterogeneity to Variability in Intrinsic Adaptation of Spiral Ganglion Neurons

Jason Boulet[1] and Ian C. Bruce[2]

[1]*McMaster Integrative Neuroscience Discovery and Study, McMaster University, 1280 Main Street West, Hamilton, ON L8S 4K1, Canada*

[2]*Department of Electrical and Computer Engineering, McMaster University, 1280 Main Street West, Hamilton, ON L8S 4K1, Canada*

Received: 15 May 2016; Accepted: 10 November 2016; Online publication: 9 December 2016

ABSTRACT

Spiral ganglion neurons (SGNs) exhibit a wide range in their strength of intrinsic adaptation on a timescale of 10s to 100s of milliseconds in response to electrical stimulation from a cochlear implant (CI). The purpose of this study was to determine how much of that variability could be caused by the heterogeneity in half-maximal activation potentials of hyperpolarization-activated cyclic nucleotide-gated cation (HCN) channels, which are known to produce intrinsic adaptation. In this study, a computational membrane model of cat type I SGN was developed based on the Hodgkin-Huxley model plus HCN and low-threshold potassium (KLT) conductances in which the half-maximal activation potential of the HCN channel was varied and the response of the SGN to pulse train and paired-pulse stimulation was simulated. Physiologically plausible variation of HCN half-maximal activation potentials could indeed determine the range of adaptation on the timescale of 10s to 100s of milliseconds and recovery from adaptation seen in the physiological data while maintaining refractoriness within physiological bounds. This computational model demonstrates that HCN channels may play an important role in regulating the degree of adaptation in response to pulse train stimulation and therefore contribute to variable constraints on acoustic information coding by CIs. This finding has broad implications for CI stimulation paradigms in that cell-to-cell variation of HCN channel properties are likely to significantly alter SGN excitability and therefore auditory perception.

Keywords: accommodation, cochlear implants (CIs), hyperpolarization-activated cyclic nucleotide-gated cation (HCN) channels, refractoriness, spike rate adaptation, spiral ganglion neuron (SGN)

INTRODUCTION

Upon receiving auditory information from inner hair cells (IHCs) in the cochlea, spiral ganglion neurons (SGNs) initiate spiking neural activity, which is then transmitted to neurons of the cochlear nucleus. If IHCs are damaged or dead, cochlear implants (CIs) provide a prosthetic solution for delivering a functional sense of hearing to individuals by electrically stimulating SGNs with patterned pulses. Studies such as the work by Arora et al. (2009) have demonstrated that speech perception is not necessarily improved by increasing the stimulation rate above 900 pulses/s/electrode (for a more comprehensive list of studies exploring the effect of pulse rate on speech perception performance refer to Boulet et al. 2016, and references therein). Adaptation may be partially responsible for the variability in speech perception by diminishing the SGN response for high-rate stimulation. A computational model that can accurately describe how SGNs respond to electrical stimulation

Correspondence to: Jason Boulet · McMaster Integrative Neuroscience Discovery and Study · McMaster University · 1280 Main Street West, Hamilton, ON L8S 4K1, Canada. email: jason.boulet@gmail.com

may provide an important tool for understanding the underlying electrophysiology of the SGN and for developing CI stimulation paradigms that take into account the operating limits and spatiotemporal interactions of SGNs (Boulet et al. 2016; Miller et al. 2003).

Adaptation can be observed in post-stimulus time histograms (PSTHs) as an ongoing decay in a neuron's firing rate. In SGN responses to CI stimulation, this phenomenon typically occurs on the order of 10 to 100 ms or more and is prevalent for a wide range of stimulation pulse rates and current levels (Heffer et al. 2010; Litvak et al. 2003; Miller et al. 2011; Zhang et al. 2007). In particular, Zhang et al. (2007) found a range of adaptation strengths in response to stimulating SGNs with high-rate pulse trains. Another study by Miller et al. (2011) showed that SGNs slowly recovered on a timescale of 10 to 100 ms after adapting to trains of high-rate stimulation. It is notable that this adaptation appears to consist of both suprathreshold adaptation, i.e., spike-dependent spike rate adaptation, and accommodation, i.e., a subthreshold stimulus-dependent drop in excitability (Boulet et al. 2016; Miller et al. 2011; Negm and Bruce 2014).

Since the Hodgkin-Huxley (HH) model (1952) does not predict spike rate adaptation, Woo et al. (2009a, b, 2010) proposed a Hodgkin-Huxley model augmented with a spike-dependent extracellular potassium accumulation mechanism that is endogenous to leech central nervous system (Baylor and Nicholls 1969). This model was extended by Miller et al. (2011) to explain accommodation (subthreshold adaptation) by including low-threshold potassium (KLT) channels characterized by two-state activation. Unfortunately, the adjustment of the nodal KLT channel densities responsible for producing realistically strong adaptation led to unrealistically long absolute refractory period (ARP) durations (Miller et al. 2011).

However, type I SGNs are endowed with a remarkable diversity of voltage-gated ion channel types that allow for various modes of excitation, including adaptation/accommodation to constant current injection (see Table 1 and Fig. 3 of Davis and Crozier 2015). Of these many channel types, the hyperpolarization-activated cyclic nucleotide-gated cation (HCN) channel has been characterized as being partially open at rest and has gating dynamics with time constants in the range of 10s to 100s of milliseconds at mammalian body temperature (Benarroch 2013; Biel et al. 2009; Howells et al. 2012; Robinson and Siegelbaum 2003). These characteristics led Negm and Bruce (2008, 2014) to propose an alternative SGN model that was capable of producing spike rate adaptation and accommodation while also generating accurate ARP values in response to CI stimulation. In their model, Negm and Bruce (2008, 2014) added HCN channels (Hugenard and McCormick 1992; Rothman and Manis 2003b) and KLT channels with activation and partial inactivation particles (or channel gating variables) that were characterized from neurons found in murine ventral cochlear nucleus (VCN) (Rothman and Manis 2003a) to the standard Hodgkin-Huxley model. Despite varying HCN and KLT channel densities, the model could only produce either no adaptation or strong adaptation, not the continuum of strengths of adaptation, i.e., from none to full strength, that is observed experimentally.

HCN channel subunits are prevalent in neurons of the lower auditory system where they function by activating under membrane hyperpolarization, being restored towards its depolarized reversal potential and deactivating under membrane depolarization, thus regulating the effective resting membrane potential (Cao and Oertel 2011; Kim and Holt 2013; Liu et al. 2014a, b; Rothman and Manis 2003a; Rusznák and Szűcs 2008). The half-maximal activation potential ($V_{1/2}$) is a parameter involved in determining a channel's voltage-dependent gating and has known heterogeneity in HCN channels. In guinea pig SGN, $V_{1/2}$ was reported as −104 mV in the afferent dendrites (Yi et al. 2010) and −101 mV at the soma (Chen 1997). The $V_{1/2}$ values reported in murinae expressed the wide range of −115 to −87 mV in the apex and −110 to −92 mV in the middle and base of the cochlea (Liu et al. 2014b, see Table 2), whereas cell-to-cell variation within a cochlear region showed a similar range (−122 to −78 mV) (Mo and Davis 1997). Finally, in neonatal mice, the half-maximal activation potential was reported in the range of −106 to −91 mV (Kim and Holt 2013).

This study sought to test the hypothesis that varying the half-maximal activation potential of the HCN model taken from murine VCN (Rothman and Manis 2003b) or a newer HCN model obtained from basal SGN (Liu et al. 2014b) impacts the strength of spike rate adaptation and accommodation in a membrane model of type I SGN. The effects of $V_{1/2}$ on refractoriness were also investigated to determine whether strong adaptation could be produced while keeping refractory behavior within the experimentally observed bounds.

METHODS

Membrane Model

The membrane potential (V_m) of a single node of Ranvier for a type I SGN was modeled in the same fashion as Negm and Bruce (2008, 2014). This model builds on the Hodgkin-Huxley-type (1952) voltage-gated fast sodium Na_v and delayed-rectifier potassium K_v channels that were modified for 37 °C (Mino et al.

2002), plus additional ionic currents described below, a leakage current I_{leak}, and the injected stimulation current I_{Inj}. In total, the four ionic currents were characterized by the fast sodium (I_{Na}) (Mino et al. 2002, 2004), delayed-rectifier potassium (I_K) (Mino et al. 2002, 2004), low-threshold potassium (I_{KLT}) (Rothman and Manis 2003a), and either one of two hyperpolarization-activated currents: $I_{h,r}$ (Rothman and Manis 2003b) or $I_{h,(q,s)}$ (Liu et al. 2014b). The I_h currents were modeled from HCN channels, where $I_{h,r}$ refers to the current generated by the HCN(r) channel model. Governed by the HCN(q,s) channel model, $I_{h,(q,s)}$ contains the two currents $I_{h,q}$ and $I_{h,s}$ (refer to (10)) that operate independently with separate activation particles and time constants (see Fig. 1a, b). The dual nature of the HCN(q,s) channel model is likely the result of HCN1 and HCN4 subunit expression in heteromeric channels or a mix of homomeric channels in one SGN (Liu et al. 2014b; Yi et al. 2010). The reversal potential of the leakage current was configured to ensure a baseline resting membrane potential of −78 mV (Mino et al. 2002; Negm and Bruce 2008, 2014) across all model variants. The dynamics of the membrane potential V_m obey the first-order differential equation

$$C_m \frac{dV_m}{dt} + I_{Na} + I_K + I_{KLT} + I_h + I_{leak} = I_{Inj} \quad (1)$$

where C_m is the membrane capacitance. The current dynamics of I_h are given in the Appendix. Experimentally derived single-channel conductance values for the I_{KLT} and I_h currents, temperature-scaling coefficients, as well as nodal densities for the corresponding channels are unknown. These values used in this study were chosen based on the modeling studies performed by Negm and Bruce (2008, 2014). In their SGN membrane model, Negm and Bruce (2014) showed that KLT and HCN channels can induce spike rate adaptation and significantly change the degree of refractoriness compared to the Hodgkin-Huxley (HH) model. However, the degree of spike rate adaptation and refractoriness was largely insensitive to the number of KLT and HCN channels (Negm and Bruce 2014). For membrane model parameter values, refer to Table 1. Six different models were simulated of which the first was the Hodgkin-Huxley model and the remaining five were HH models augmented with ionic currents and are denoted by their channel type: (2) +HCN(r), (3) +HCN(q,s), (4) +KLT, (5) +HCN(r) + KLT, and (6) +HCN(q,s) + KLT. Refer to next section on "Modifications to Kinetic HCN Channel Models" for descriptions of the HCN(r) and HCN(q,s) channel models.

The effect of voltage-gated ion channel stochasticity on the membrane potential is inversely related to the neuron's diameter (Verveen 1962; Verveen and Derksen 1968) and since type I SGN axons are relatively small, the fluctuations contribute to the total membrane response in a significant way (Imennov and Rubinstein 2009; Rubinstein 1995). The effects of single-cell stochasticity also provide better predictions than deterministic models of some psychophysical (Bruce et al. 1999a). Therefore, it is important to accurately model the stochastic nature of voltage-gated ion channels since the resulting membrane fluctuations are one of the main sources of spike timing variability (Schneidman et al. 1998).

Voltage-gated ion channel states were simulated with an efficient and exact version of Gillespie's direct method (Gillespie 1977) for Markov chains known as the channel number tracking procedure (Mino et al.

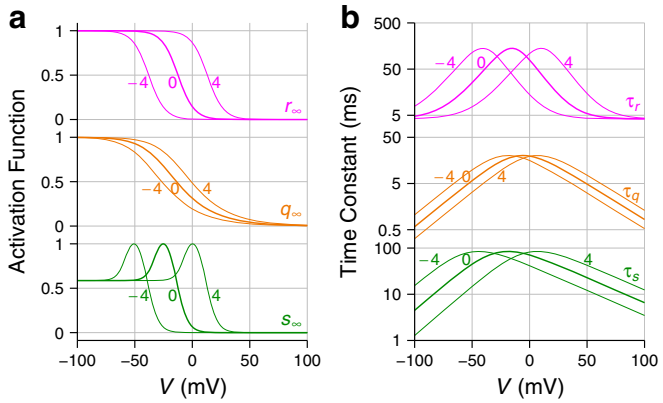

FIG. 1. **a** Activation functions and **b** time constants for the HCN(r) and HCN(q,s) channel models as a function of the relative membrane potential V. Several *curves* are shown for each HCN model, including one *bold line* that represents the non-shifted model and two *thinner lines* that indicate the minimum and maximum of the explored ranges. *Numbers* shown beside the curves indicate how many $V_{1/2}$ standard deviations the functions have been shifted by. Refer to (8, 9), and (12–17) for more details.

TABLE 1

SGN node of Ranvier membrane model parameters

Parameter	*Symbol*	*Value*	*Reference*
Nodal capacitance	C_m	0.0714 pF	Bruce (2006)
Nodal resistance	R_m	1953.49 MΩ	Bruce (2006)
Na reversal potential	E_{Na}	66 mV	Mino et al. (2002)
K reversal potential	E_K	−88 mV	Mino et al. (2002)
HCN(r) reversal potential	$E_{h,r}$	−43 mV	Rothman and Manis (2003b)
HCN(q,s) reversal potential	$E_{h,(q,s)}$	−41 mV	Liu et al. (2014b)
Resting membrane potential	V_{rest}	−78 mV	Mino et al. (2002)
Na_v conductance	γ_{Na}	25.69 pS	Mino et al. (2002)
K_v conductance	γ_K	50.0 pS	Mino et al. (2004)
KLT conductance	γ_{KLT}	13.0 pS	Negm and Bruce (2014); text
HCN conductance	γ_h	13.0 pS	Negm and Bruce (2014); text
Max# Na_v channels	N_{Na}^{max}	1000	Mino et al. (2002)
Max# K_v channels	N_K^{max}	166	Negm and Bruce (2014); text
Max# KLT channels	N_{KLT}^{max}	166	Negm and Bruce (2014); text
Max# HCN(r) channels	$N_{h,r}^{max}$	100	Negm and Bruce (2014); text
Max# HCN(q) channels	$N_{h,q}^{max}$	$p_q N_{h,r}^{max}$	Liu et al. (2014b); Negm and Bruce (2014)
Max# HCN(s) channels	$N_{h,s}^{max}$	$p_s N_{h,r}^{max}$	Liu et al. (2014b); Negm and Bruce (2014)
Proportion HCN(q) channels	p_q	0.4471	Liu et al. (2014b)
Proportion HCN(s) channels	p_s	$1 - p_q$	Liu et al. (2014b)
KLT thermal coefficient	$Q_{10,KLT}$	3.0	Negm and Bruce (2014); text
HCN thermal coefficient	$Q_{10,h}$	3.3	Negm and Bruce (2014); text
HCN(r) $V_{1/2}$ standard deviation	σ_r	6.37 mV	Liu et al. (2014b); text
HCN(q) $V_{1/2}$ standard deviation	σ_q	3.20 mV	Liu et al. (2014b)
HCN(s) $V_{1/2}$ standard deviation	σ_s	6.37 mV	Liu et al. (2014b); text

2002). Over a simulation interval or time step, the channel number tracking procedure performs stochastic updates of the number of channels in each channel state such that the probability of transitioning between adjacent channel states is dependent on the transition rate of that state transition and the number of channels in that state. All channel models were first initialized at resting membrane potential in order to randomize channel states over a period long enough (300 ms, see Fig. 1b) to capture the kinetics of even the slowest model, where the maximum τ_r is 140.8 ms. Next, the membrane model was initialized for 300 ms with I_{inj} = 0 pA, allowing the membrane potential to fluctuate naturally prior to the membrane model being exposed to stimulation paradigms. The simulation of the membrane model (1) was solved by the explicit Euler method using time steps of 1 μs. Code for the simulation and analysis of the membrane models may be found at ModelDB.

Modifications to Kinetic HCN Channel Models

In this study, the half-maximal activation potential ($V_{1/2}$) of the two HCN kinetic models were varied to determine the operational range of the channel in terms of its ability to slowly modulate the voltage response of the neural membrane. Following Negm and Bruce (2014), the HCN(r) model was first adjusted to account for the difference in the resting membrane potential of the VCN cell model of Rothman and Manis (2003b) and that of the SGN cell model. Since the HCN(q,s) model was already characterized from murine SGN, the assumption was made that the resting membrane potential is similar between murine and feline SGNs. Figure 1 shows the activation functions and time constants (as a function of the relative membrane potential V, which is the membrane potential V_m relative to the resting membrane potential V_{rest}, or $V = V_m - V_{rest}$) at their mean $V_{1/2}$ HCN models (bold curves).

The basal cochlear HCN(q,s) channel model contains two parallel conductances that operate at distinct timescales. The "quick" q particle's $V_{1/2}$ standard deviation is 3.20 mV (Liu et al. 2014b). The activation of the "slow" s particle (s_∞) is described by two Boltzmann equations (refer to (13) and (14) in the Appendix) and is characterized by the $V_{1/2}$ standard deviations: 4.34 and 8.40 mV (Liu et al. 2014b). In order to simplify shifts in s_∞ and τ_s without distorting the shape of the activation functions, both of the s particle's components were shifted by integer multiples of the mean value, 6.37 mV instead of shifting each component by their separate values. As for the HCN(r) channel description, its activation function r_∞ and time constant τ_r were shifted by the same value (6.37 mV) in order to simplify the comparison of the relative effects of HCN channel type.

A range of $V_{1/2}$ shifts were systematically applied to the HCN kinetic models. These shifts were

defined as $cV_{1/2}$ standard deviations, where c is an integer. Shifts were explored over ±4 $V_{1/2}$ standard deviations, because of some uncertainty as to the direct applicability of the $V_{1/2}$ statistics from cultured, neonatal, murine SGNs to this study's model of in vivo responses of adult, feline SGNs, as well as uncertainty about the resting membrane potential of murine SGNs. Figure 1 shows the shifts applied to both the activation functions and the time constants as a function of the relative membrane potential. The activation function is defined as the steady-state probability of a channel activation or inactivation particle being open as a function of the (relative) membrane potential. The activation function of each particle is shown in Figure 1a and is shifted by specific integer multiples (shown beside the curves) of the $V_{1/2}$ standard deviation. Figure 1b shows the time constant, shifted by the same values as the activation function. The HCN(r) and HCN(q,s) model functions were shifted by −4, −3, −2, −1, 0, 1, 2, 3, and 4 standard deviations of $V_{1/2}$. When referring to a model variant with shifted kinetics, such as +HCN(q,s) + KLT that has its HCN(q,s) kinetics shifted by $cV_{1/2}$ standard deviations, the convention used throughout is: +HCN(q,s,c) + KLT.

Stimuli

In this simulation study, the pulse amplitude of the adaptation, masker-probe train recovery, and refractoriness stimulation paradigms was quantified in terms of the firing efficiencies (FEs) specific to each neuron model. The FE corresponds to the probability that the neuron will spike due to being driven by a single pulse at a specific current level. A firing efficiency of 50 % corresponds to the average single-pulse threshold current. The stimulation parameters varied somewhat across the studies from which the data were taken to evaluate the modeling results. In order to reduce the number of simulations required, a consistent set of stimulation parameters were chosen that are close to, but do not all exactly match, the parameters used in the experimental studies. In contrast to studies that use CI stimulation, where current is applied in the extracellular space of SGNs; in this study, all stimulation was provided by intracellular current injection with the intention of efficiently initiating responses at the membrane.

A 200-ms train of high-rate pulses was initially used by Miller et al. (2011) as a forward masker to determine its effect on the subsequent neural recovery in response to a 250-ms low-frequency probe pulse train. Two types of stimuli trains were generated: (1) probe-alone and (2) masker-probe, where the probe-alone case represented the masker-free control condition. In this study, each masker and probe train lasted for 300 ms, held a fixed pulse current level, and directly followed each other. For the probe-alone train, the masker train was delivered at I_{inj} = 0 pA. In these simulations, the masker-probe train began with a masker train and was delivered at a variety of first-pulse FEs (1, 10, 20, 50, 80, 99, 99.99, and 99.9999 %) and pulse rates (200, 800, 2000, and 5000 pulses/s) (Miller et al. 2008, 2011; Negm and Bruce 2008, 2014; Zhang et al. 2007). The high FEs, i.e., 99.99 and 99.9999 % were chosen to emulate the highest current levels of Miller et al. (2011), which, respectively, were approximately 0.9 and 1.3 dB greater than the lowest current level to elicit at least one spike in response to the masker pulse train interval. In all cases, the probe train was delivered at the single-pulse threshold current level and 100 pulses/s (Miller et al. 2011). Each pulse was a biphasic, symmetric, depolarizing-phase-leading pulse that lasted 50 μs/phase without an interphase gap (Negm and Bruce 2014). The durations of the 200-ms masker train and the 250-ms probe train from the Miller et al. (2011) study are different from the 300-ms masker and probe train durations used in this study. The reason for these differences was to compare pulse train response from the Zhang et al. (2007) study (300-ms pulse train durations) by analyzing the masker train responses from this study. Essentially, the stimuli for studying onset adaptation were just the initial masker portion of the masker-probe pulse trains, without the probe.

In order to determine the refractory behavior, a paired-pulse paradigm (Cartee et al. 2000, 2006; Dynes 1996; Miller et al. 2001) was adopted that was designed to establish the current amplitude of a second pulse required to elicit a spike, given that the neuron always spiked in response to the first pulse. More specifically, the pulses were separated in time by an interpulse interval (IPI) (Cartee et al. 2000, 2006; Dynes 1996; Miller et al. 2001; Negm and Bruce 2014). The first-pulse I_{inj} amplitude was set to a value equivalent to an FE of 99.9 %, where only cases that elicited a spike in response to the first pulse were collected. The second pulse was separated from the first pulse by a range of IPIs, each with various current levels to determine the operational range of FEs as a function of the IPI. Similarly to Miller et al. (2001), each pulse was monophasic, but with a 50-μs duration.

Analysis

Since the model neurons are stochastic, their probability of firing for any given stimulation current level can be predicted by a cumulative distribution function. Studies have shown that the Gaussian cumulative distribution (Φ), as a function of the injected current

(I_{inj}) (Bruce et al. 1999b; Verveen and Derksen 1968) can accurately predict the probability of firing or the firing efficiency

$$FE(I_{inj}) = \Phi\left(\frac{I_{inj}-\theta}{\sigma}\right) \quad (2)$$

where θ is the threshold current and σ determines the dynamic range. Typically, the neuron's dynamic range is reported in a normalized fashion as the relative spread (RS) = σ/θ (Verveen and Derksen 1968). Since the threshold current and relative spread is sensitive to the exact mixture of voltage-gated ion channels, they help define a stimulus current scale that is calibrated to each model neuron variant. For each such model neuron variant, the single-pulse threshold (θ_{SP}) and single-pulse relative spread (RS_{SP}) was estimated. This was done by fitting the outcomes of 1000 simulation trials across a range of injected current levels to (2), where the current waveforms consisted of 50-μs duration monophasic and biphasic pulses. Due to the discrete, binary nature of whether a neuron spikes or not, the quality of all fits (2) to the spike data were evaluated by the R^2_{count} measure (Long 1997).

Post-stimulus time histograms were calculated over 500 simulation trials for the masker-probe train responses and for the adaptation responses. The response rate (or spike rate), captured by the PSTHs was computed as the number of spike occurrences within a given time bin, divided by the bin interval and the number of trials. PSTHs were evaluated for narrow bins of 1 ms and a wide interval axis where the bins are 0–4, 4–12, 12–24, 24–36, 36–48, 48–100, 100–200, and 200–300 ms, as in Zhang et al. (2007). Several features were extracted from the response rate as a function of time: (1) onset rate, (2) normalized spike rate decrement (NSRD), (3) adaptation time constant (τ_{adapt}), (4) probe response recovery ratio (PRRR), and (5) the mean response rate to the masker. The onset rate is just the response rate over the 0–12-ms interval (Zhang et al. 2007). The NSRD is the spike rate decrement divided by the onset rate where the spike rate decrement is the onset rate subtracted by the final rate (or the rate corresponding to the 200–300-ms bin) (Zhang et al. 2007). One adaptation time constant τ_{adapt} was extracted by fitting the PSTH simulation results to $\rho(t)$, a decaying exponential function

$$\rho(t) = A_{ss} + A_{dec}\exp\left(-t/\tau_{adapt}\right) \quad (3)$$

where A_{ss} and A_{dec} are estimates of the steady-state rate and the spike rate decrement, respectively. Whereas Zhang et al. (2007) tested decaying exponential fits with both one and two time constants, it was found that one time constant was sufficient, as reported by an R^2 value. Note that τ_{adapt} refers to the overall time-course of the drop in spike rate and is influenced by refractoriness, facilitation, and accommodation (subthreshold adaptation) in addition to spike-dependent spike rate adaptation (Boulet et al. 2016). The PRRR is the ratio of probe response spikes in the masker-probe condition to the probe-alone condition (Miller et al. 2011). Finally, the mean response rate to the masker was calculated simply as the time-averaged response rate over the entire masker train interval of 300 ms.

In the refractory function analysis, the ratio of the masked (second) pulse threshold (θ_{ref}) to the unmasked or single-pulse threshold (θ_{SP}) was reported as a function of the interpulse interval. The number of trials varied as a function of the interpulse interval such that at the minimum IPI there were 500, whereas at the maximum IPI, there were 100. This procedure was carried out to obtain better estimates of the absolute refractory period and the relative refractoriness immediately following the absolute refractory period. Miller et al. (2001) found that a significant proportion of SGNs exhibited an extended relative refractory period in their refractory threshold ratio data. In order to address this need to capture more than one timescale in the refractory response, the approach introduced by Negm and Bruce (2014) was adopted that generalizes the refractory threshold ratio function to two time constants

$$\frac{\theta_{ref}}{\theta_{SP}} = \frac{\sum_{i=1}^{2} A_i}{\sum_{i=1}^{2} A_i[1-\exp(-(IPI-\Delta t_{abs})/\tau_i)]} \quad (4)$$

where Δt_{abs} is the ARP, τ_1 and τ_2 are the relative refractory period (RRP) time constants, and A_1 and A_2 are corresponding strengths.

Spike Detection

The detection of spikes by comparing the relative membrane potential to a sufficiently elevated fixed relative membrane potential crossing level of say 100 mV may be adequate in response to single-pulse stimulation. In multi-compartmental models of a full neuron, any impulse that propagates to the end of the axon is recognized as a spike and thus spike detection is a trivial task. However, high-rate (short IPI) and large-amplitude (beyond the neuron's dynamic range) multiple stimuli present unique challenges for spike detection for non-spatially distributed neural models.

Passive charging of the membrane potential in response to large-amplitude pulses may visually appear to be artifacts, yet may still cross an arbitrary threshold, resulting in the false classification of spiking. This scenario is common with refractory stimuli in response to the second (or probe) pulse (refer to the amplitude/unmasked amplitude or bottom panel of Fig. 6 in Miller et al. 2001) due to the depletion of open sodium channels in response to a spike driven by the first (or masker) pulse. At the onset of the second pulse, few sodium channels are ready for voltage-dependent activation which results in a major capacitive current (thus, large passive charging, or fixed-point dynamics) and a minor sodium current. In contrast, if the sodium current participates in a positive feedback loop with the membrane potential, a limit cycle forms (Guevara 2003), which is the hallmark of Hodgkin-Huxley action potential (AP) generation. Thus, the sodium activation may result in a relatively long-lasting, self-sustaining event known as a spike (or AP), or may create a passive response that is pulse-width-dependent in duration.

Therefore, it was hypothesized that spikes could be accurately predicted by some value of λ, the sodium conduction duration, defined as the period of time for which the proportion of open sodium channels is greater than 0. Where $N_{m_3h_1}(t)$ is the number of Na channels in the open or conducting state (m_3h_1, in the Hodgkin-Huxley channel formalism) at time t, the set of λs (collected over multiple trials and current levels) occurring over the interval $0 \leq t \leq T_{\text{stim}}$ can be written as

$$\{\lambda\} \triangleq \text{duration}\left(\frac{N_{m_3h_1}(t)}{N_{\text{Na}}^{\max}} > 0\right) \tag{5}$$

where $N_{\text{Na}}^{\max}$ is the number of Na_v channels and T_{stim} is the stimulus interval. Figure 2b shows examples of the sodium conductance duration λ for the HH and +HCN($q,s,4$) + KLT model variants. In this scenario, when stimulated with a 50-μs monophasic single-pulse set to a FE of 99.9 %, the +HCN(q, s, 4) + KLT model achieves a lower median value of λ. When stimulated over a wide range of current levels, Figure 2c shows that a bimodal distribution of λ emerges, suggesting that a threshold θ_λ can be determined such that values which are greater may be classified as action potentials instead of smaller sodium fluctuations.

In order to determine θ_λ, the neural response was first simulated with independent single pulses at 200 linearly spaced current levels spanning the range 0 to 150 pA. Each stimulus was presented for a total of 1000 trials per current level. For every trial, the maximum λ was collected. The set of all λs, $\{\lambda\}$ was then aggregated over all current levels and trials. Next, $\{\lambda\}$ was clustered into two groups: $\{\lambda_1\}$ containing small values and $\{\lambda_2\}$ composed of all values greater than those in $\{\lambda_1\}$. This was performed by a method known as Jenks natural breaks optimization (Jenks 1967), which is equivalent to k-means clustering for 1-dimensional data. Following this, θ_λ was defined as a value in $\{\lambda_2\}$ equal to the 0.1 percentile of $\{\lambda_2\}$. This step was performed to minimize false spike detection due to possible crossover of the tails of the λ_1 and λ_2 distributions since those distributions were not known a priori. For all single-pulse, adaptation, masker-probe train, and refractory simulations, action potentials were identified if $\lambda \geq \theta_\lambda$.

RESULTS

Single Pulse

Simulation results shown in Figure 3 establish the monophasic and biphasic single-pulse statistics for all neuron model variants as a function of the shift in HCN half-maximal activation potential (Fig. 3a sodium conductance duration threshold, Fig. 3b AP threshold current, and Fig. 3c relative spread). Results for the HH and +KLT models appear constant as a function of c since no HCN channels are included in those models. However, all models that do contain HCN display a deceasing θ_λ as a function of c. This is due to (1) an increased total resting membrane conductance and (2) an increased rate of repolarization produced by HCN deactivation following depolarization.

Due to the increased total resting membrane conductance, the single-pulse threshold currents increase with respect to c for models with HCN channels. Just as previously reported (Liu et al. 2014a; Negm and Bruce 2008, 2014), KLT shows an increase of θ_{SP} relative to HH in the +KLT model and an additive effect to θ_{SP} in models with HCN. Whereas Negm and Bruce (2014) used a threshold-crossing value of 80 mV relative to rest; in this study, θ_λ was used to detect action potentials. For the models HH, +HCN(r, 0), +KLT, and +HCN(r, 0) + KLT models, Negm and Bruce (2014) reported the respective biphasic single-pulse thresholds 54.29, 59.68, 57.36, and 62.70 pA in contrast to values from this study: 55.70, 60.74, 58.80, and 63.88 pA.

For both monophasic and biphasic stimulation, the +KLT model shows a greater relative spread than the HH model, indicating a greater dynamic range in response to single pulses, consistent with Negm and Bruce (2008). The +HCN(r) and +HCN(q,s) models maximize the RS_{SP} at $c = 0$. In contrast, the +HCN(r) + KLT and +HCN(q,s) + KLT models show a constant

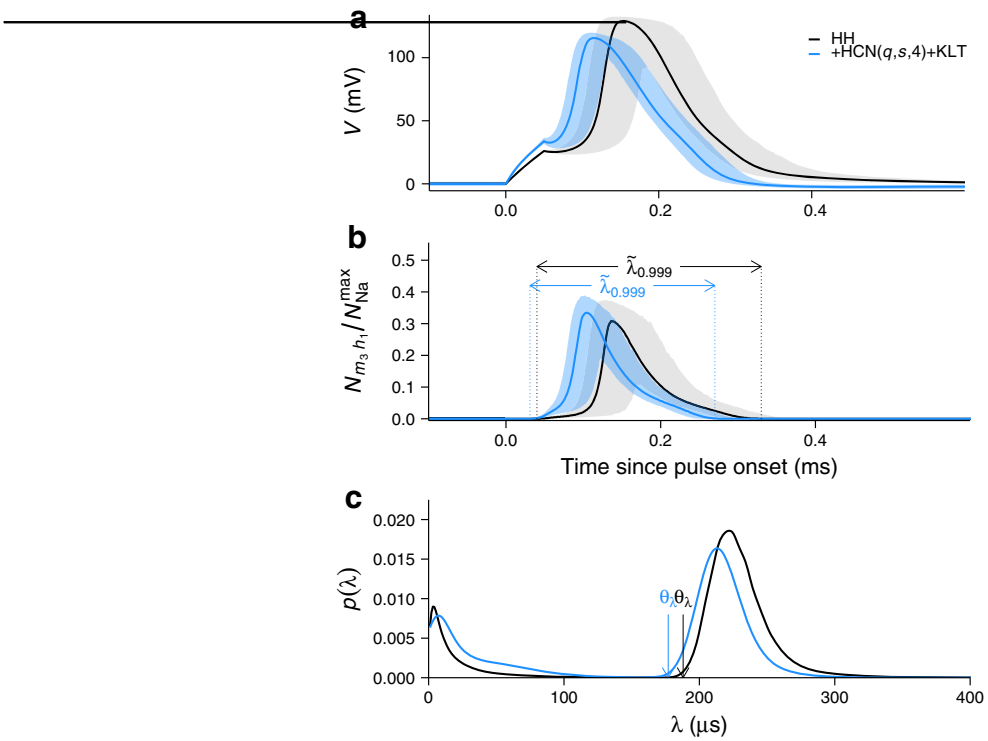

FIG. 2. Determination of a spiking threshold based on the sodium conductance duration λ. The HH model is shown in *black*, the +HCN($q, s, 4$) +KLT model is shown in *light blue*. **a**, **b** Data represent 1000 independent responses to a 50-μs monophasic single pulse delivered at a current level equivalent to a FE of 99.9 %. **a**, **b** Data on the ordinate axes have been summarized by median values (*solid line*) and the lower 2.5 and upper 97.5 percentiles (*shaded area*). **a** Relative membrane potential (V). **b** Proportion of open sodium ion channels ($N_{m_3h_1}/N_{\mathrm{Na}}^{\mathrm{max}}$). $\tilde{\lambda}_{0.999}$ denotes the median sodium conductance duration, or the median duration over which $N_{m_3h_1}/N_{\mathrm{Na}}^{\mathrm{max}} > 0$ given a stimulus FE of 99.9 %. **c** Empirical probability density of λ marginalized over all stimulus current levels. Values to the *left* of θ_λ represent sodium conductances that are either failed action potentials or short-lived sodium fluctuations whereas the distribution that lies to the right of θ_λ represents values of λ which were sufficient to generate a spike. Thus, the threshold θ_λ is said to be the minimum value of λ required to generate an action potential.

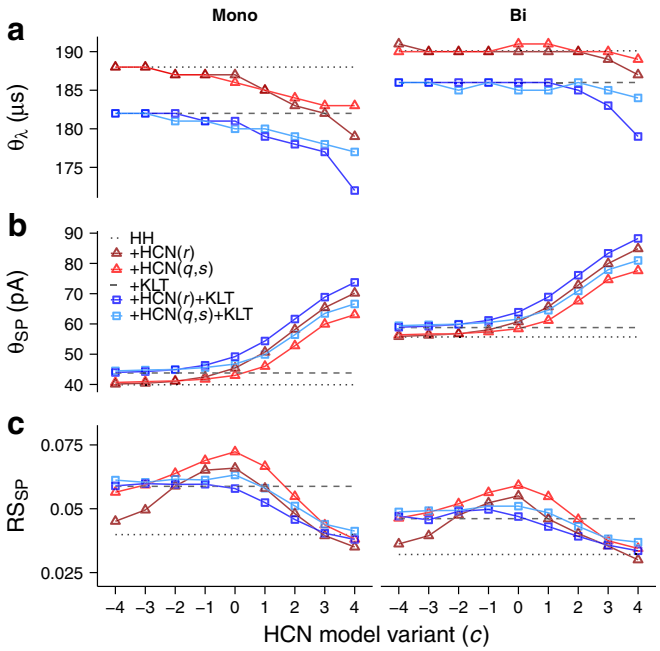

FIG. 3. Monophasic and biphasic single pulse. **a** Sodium conductance duration thresh old (θ_λ), **b** AP threshold current (θ_{SP}). **c** Relative spread ($\mathrm{RS}_{\mathrm{SP}}$) as a function of the HCN $V_{1/2}$ shift parameter c.

RS_{SP} for $c \leq 0$ approximately equal to the +KLT model, whereas for $c > 0$, RS_{SP} tends towards the HH model value. The quality of fits to (2) was quantified by R^2_{count} with the +HCN($q, s, 0$) model responding to monophasic stimulation having the lowest value R^2_{count} = 0.823 and the +HCN(r, 4) + KLT model in response to biphasic pulses having the highest R^2_{count} = 0.925.

Adaptation

Changes in the excitability of feline SGNs driven by ongoing electrical pulsatile stimulation come in a few forms that often overlap temporally (for a review, refer to Boulet et al. 2016). Examples of the decay in the response rate are illustrated by the white line-dot curves in Fig. 4. Here, feline SGNs respond to the various stimulation rates and each to a variety of pulse current levels. This phenomenon is typically referred to as having arisen due to spike rate adaptation, which has a spike-dependent nature. Upon closer examination, Figure 4c (middle row) shows that a neuron firing in response to a 5000 pulses/s pulse train also shows the effects of refractoriness, which can be observed by the oscillatory response in the PSTH for the first few pulses at least. This can be explained by a strong spiking response at the onset of the pulse train putting the neuron in a refractory state for the next pulse in most trials, such that it does not often respond to that second pulse. Subsequently, the spike rate is large again for the third pulse but reduced for the fourth pulse, and so on. An increase in the spike rate produced by facilitation is also apparent when comparing Figure 4c to Figure 4a, b, and d. Finally, clear evidence of accommodation or subthreshold adaptation is apparent in Figure 4d during the interval in which the SGN is not spiking. Since the neuron ceases spiking in the presence of ongoing pulse train stimulation, spike rate adaptation cannot be responsible for this type of drop in excitability. Therefore, accommodation must be a contributing process. However, the question remains as to what is the primary biophysical contributor to reducing electrical excitability in SGNs.

Changing the HCN half-maximal activation potential affects the pulse train response in terms of varying neuronal excitability or the strength of adaptation. Figure 5 clearly demonstrates this point for pulse train stimulation with amplitude FE = 80 % and rate of 2000 pulses/s for models +HCN(r) and +HCN(q, s), where the strength of adaptation increases as a function of c.

Figure 6 shows the probability of activation or inactivation of stochastic gating particles for the HCN(q, s) channel ($\hat{q}$ and $\hat{s}$) and the KLT channel ($\hat{w}$ and $\hat{z}$) in response to 2000 pulses/s biphasic pulse

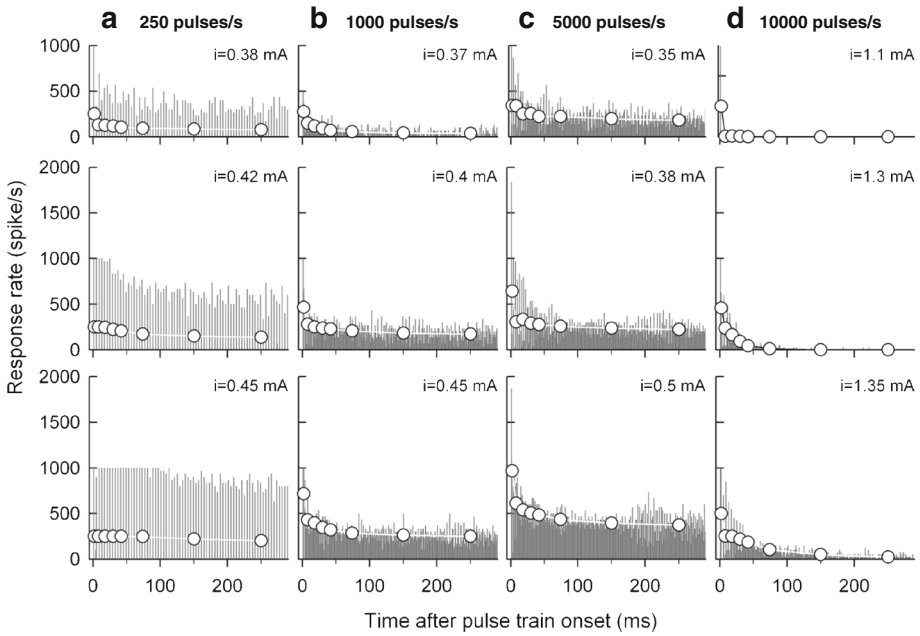

FIG. 4. Feline SGN response rate as a function of the time since pulse train onset over a 300-ms interval. Subpanels with columnar arrangement indicate responses to stimulation at the rates of **a** 250 pulses/s, **b** 1000 pulses/s, **c** 5000 pulses/s, and **d** 10000 pulses/s. Row-wise layout of the subpanels show an increasing biphasic pulse current level starting from the *top panel* to the *bottom panel*. **a**–**c** Responses were taken from a different SGN (**d**). *Bars* represent the response rate over 1-ms intervals and *dots* show the response rate over the progressively wider intervals (0–4, 4–12, 12–24, 24–36, 36–48, 48–100, 100–200, and 200–300 ms). This figure was adapted with kind permission of Springer Science and Business Media: Fig, 2 from Zhang et al. (2007), ©2007.

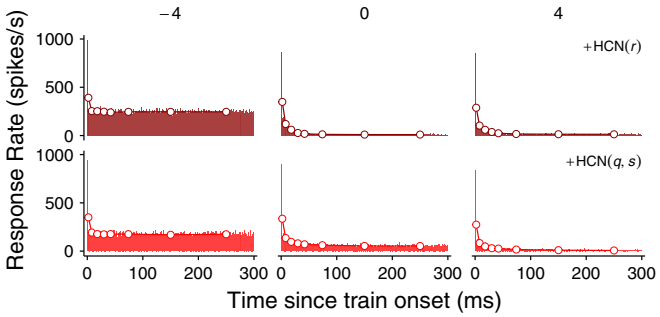

FIG. 5. PSTH responses to pulse train stimulation over a 300-ms interval at an FE of 80 % and rate of 2000 pulses/s for models +HCN(*r*) and +HCN(*q*, *s*) showing various strengths of adaptation as a function of the HCN $V_{1/2}$ shift parameter *c*. *Bars* and *dots* represent the same intervals as in Figure 4.

train stimulation. Figure 6a shows the responses to the +KLT + HCN($q,s,0$) SGN model and Figure 6b exhibits the responses to the stronger-adapting +KLT + HCN($q,s,4$) model. It is clear that since $\hat{q}$ and $\hat{s}$ are more open at rest (from 0 to 10 ms) when $c = 4$ relative to $c = 0$, the +KLT + HCN($q,s,4$) is capable of progressive membrane hyperpolarization, which gradually drives the neuron to adapt over the duration of the stimulation (cf. Fig. 5 of Negm and Bruce 2014). Due to its low-threshold regime, the stochastic activation particle of the KLT channel, $\hat{w}$ undergoes an HCN-*c*-dependent drop in activation over the stimulation interval (in Fig. 6b compared to Fig. 6a). In a similar fashion, the inactivation particle of the KLT channel, $\hat{z}$ slowly inactivates.

Figure 7 shows the PSTH responses for the six membrane models over the 20, 50, and 80 % FEs and all stimulation rates. The +HCN($r,3$), +HCN($q,s,4$), +HCN($r,3$) + KLT, and +HCN($q,s,4$) +KLT kinetic variants in Figure 7 are the strongest-adapting models with HCN channels (see Fig. 8b, NSRD). Overall, the PSTHs display a relatively high onset rate that is followed by a gradual drop down to a lower steady-state response rate. On aggregate, both onset and final spike rates are higher as a function of the firing efficiency. However, the final spike rates are not linearly predicted by pulse rate, which can be seen by the wide bin dots.

Across all firing efficiencies for models without HCN channels, the final spike rate is maximized at 800 pulses/s and decreases in response to greater stimulation rates with the exception of the HH model. Models with HCN channels show a maximum final response rate for stimulation at 200 pulses/s, which then decreases monotonically with the pulse rate. The drop in the response rate for the HH model at stimulation rates including and above 800 pulses/s occurs immediately after 1 ms and thus is not representative of adaptation but rather refractoriness. The +KLT model behaves similarly to the HH model at the 200 and 800 pulses/s stimulation rates. However, at 2000 pulses/s, the response rate is lower, and at 5000 pulses/s, the neuron does not respond except to the first pulse, indicating accommodation (subthreshold adaptation). Models containing HCN channels respond similarly to the +KLT model in

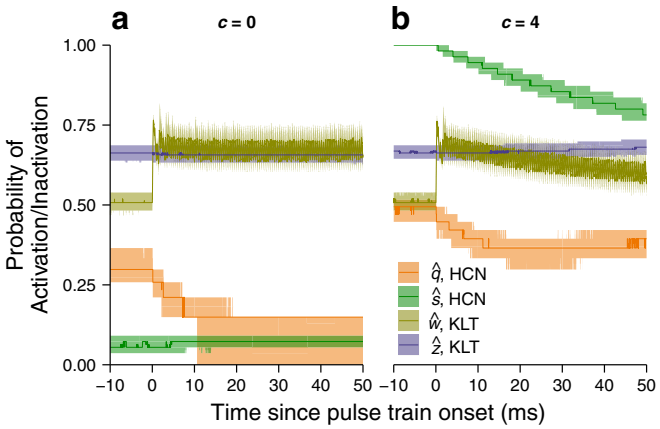

FIG. 6. Changes over time to the probability of activation or inactivation of stochastic gating particles of the HCN(q,s) channel: $\hat{q}$ (quick activation; *orange*), $\hat{s}$ (slow activation; *green*), and the KLT channel: $\hat{w}$ (activation; *yellow*), and $\hat{z}$ (inactivation; *purple*) for the **a** +KLT + HCN($q,s,0$) and **b** +KLT + HCN($q,s,4$) SGN models in response to pulse train stimulation. The SGN models were presented with 1000 trials of 50 ms of biphasic pulse train stimulation, at a rate of 2000 pulses/s and for pulse amplitudes of FE = 99.99 %. The median responses of the stochastic gating particles are drawn with solid traces, whereas the 25 to the 75 percentiles are shown as areas with *lighter colors*.

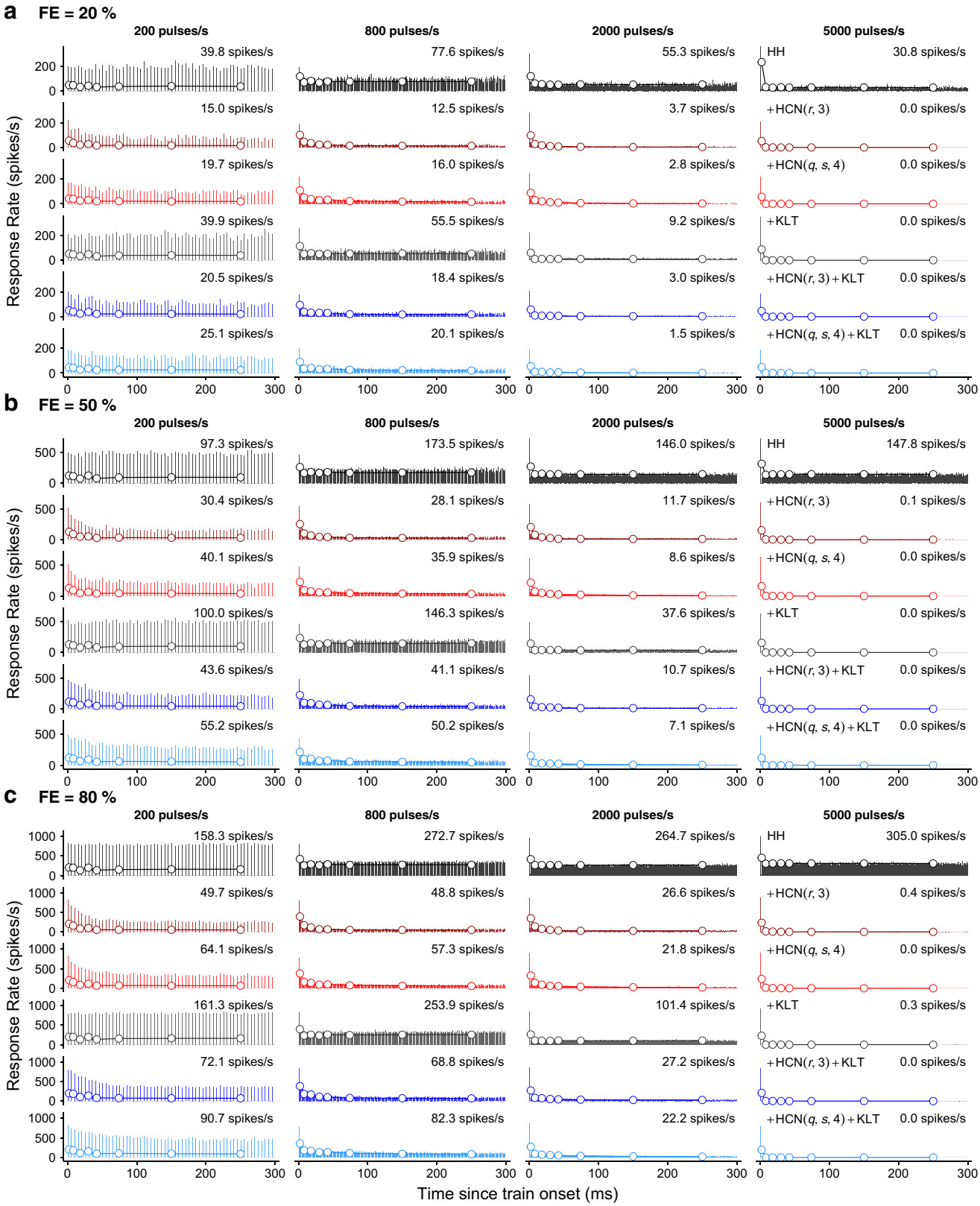

FIG. 7. PSTH or response rate for the strongest-adapting SGN membrane models over a 300-ms interval where *c* was set to give strong adaptation in the model versions containing HCN channels. *Panels* represent responses to individual FEs: **a** 20 %, **b** 50 %, and **c** 80 %. *Row subpanels* indicate membrane model and *column subpanels* represent stimulation rate. *Bars* and *dots* represent the same intervals as in Figures 4 and 5. Response rates for the last 100 ms of stimulation are reported with text above the later part of each PSTH.

terms of onset and final response rates but appear to display adaptation behavior across a broad set of stimulation rates exhibited by the relatively slower decay in the PSTH. Overall, wide bin response rates were well predicted by (3) since the worst fit was model variant +HCN(r,–4) + KLT (R^2 = 0.819) and the best fit was model variant +HCN(r, 3) (R^2 = 0.980).

Figure 8 contains simulation results that summarize the pulse train responses over the range of HCN half-maximal activation potentials (varied by c). Figure 8 also shows simulation results from this study and experimental results from Zhang et al. (2007) of the normalized spike rate decrement (NSRD) versus the onset response rate. Figure 8a shows the onset rate, Figure 8b displays the normalized spike rate decrement (NSRD), and Figure 8c reports the adaptation time constant (τ_{adapt}). Simulation results in Figure 8a–c (onset rate, NSRD, and adaptation time constant) were averaged over all FEs (1, 10, 20, 50, 80, 99, 99.99, and 99.9999 %) and the pulse rates (200, 800, 2000, and 5000 pulses/s). "Strong-adapters" were defined as the neurons with NSRD greater than 0.75, just as in Negm and Bruce (2014), and can be seen in the light gray zone (in Fig. 8b). Out of all membrane models and their respective shifted $V_{1/2}$ HCN variants, the following are classified as strong adapters: +HCN(r,1), +HCN(r,2), +HCN(r,3), +HCN(r,4), +HCN(q,s,4), +HCN(r,2) +KLT, +HCN(r,3) +KLT, +HCN(r,4) +KLT, and +HCN(q,s,4) +KLT. Notably absent from the list of strongly adapting neurons are the HH and +KLT models, indicating that HCN channels are required to produce strong adaptation.

All models containing the KLT channels have a distinctly lower onset response rate in Figure 8a than those without, and thus KLT appears to be a strong regulator of the onset response rate. Since the onset response rate is calculated over 0–12 ms and the drop in the firing rate occurs 1 ms after the onset of the

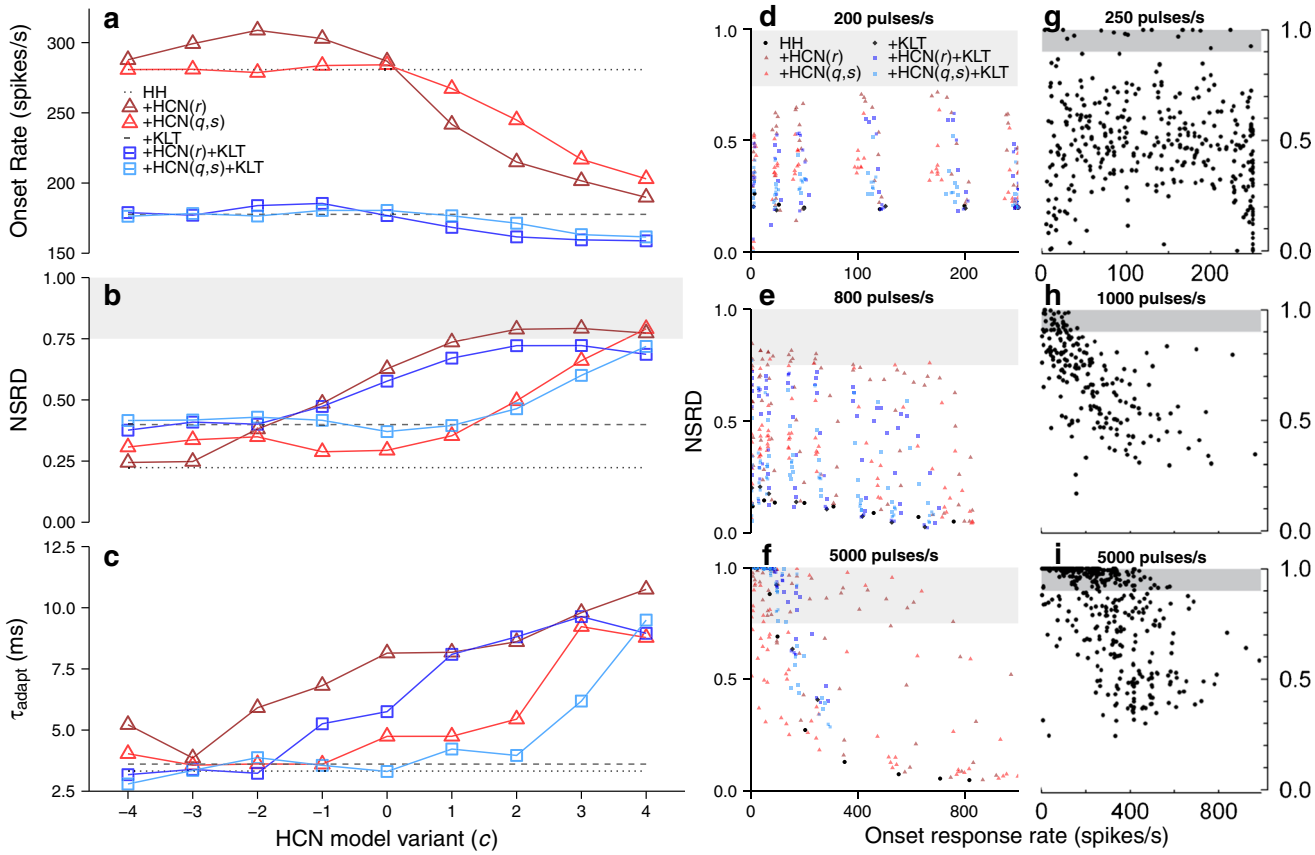

FIG. 8. Summary of the pulse train response statistics. Pulse train responses for all SGN model variants given by **a** onset rate, **b** NSRD, and **c** τ_{adapt}, as a function of the HCN $V_{1/2}$ shift parameter c. Note that the HH and +KLT models are, respectively, represented by flat *dotted* and *dashed lines* (**a**–**c**) since they do not contain HCN channels and therefore cannot vary with c. Simulation results (**a**–**c**) were averaged over all FEs (1, 10, 20, 50, 80, 99, 99.99, and 99.9999 %) and all pulse rates (200, 800, 2000, and 5000 pulses/s). SGN model simulation results for NSRD as a function of the onset response rate in response to pulse train stimulation at the **d** 200 pulses/s, **e** 800 pulses/s, and **f** 5000 pulses/s rates. **d**–**f** Simulation results across all HCN $V_{1/2}$ levels (−4 to 4) and FEs (1, 10, 20, 50, 80, 99, 99.99, and 99.9999%). The remaining panels correspond to the same NSRD versus onset response rate simulation plots, but for feline SGN recordings (Zhang et al. 2007) responding to **g** 250 pulses/s, **h** 1000 pulses/s, and **i** 5000 pulses/s pulse train stimulation. Note that the span of the onset response rate (**d**, **g**) is 0 to 250 spikes/s and (**e**, **f**, **h**, **i**) is 0 to 1000 spikes/s. **g**–**i** Adapted with kind permission of Springer Science and Business Media: Figure 5b, e, g from Zhang et al. (2007), © 2007.

pulse train (see Fig. 7), this could be related to processes other than spike rate adaptation, such as refractoriness. However, as seen in Figure 7, the HH and +KLT models have a relatively high final response rate, with the HH response being the highest. This may help explain the disparity in the NSRD between the HH and KLT-containing models. Models with HCN but without KLT channels cover a wide set of onset response rates ranging from approximately 190 to 310 spikes/s near the HH response. Onset response rates of the HCN models that are near the HH response can be explained by the HCN channels being closed at (and somewhat below) the resting membrane potential, specifically the r_∞ and the slow s_∞ component (see Fig. 1a). In terms of the positively shifted $V_{1/2}$ HCN model variants, the r and s particles are at least half open at the resting membrane potential and are in a position to strongly restore the membrane potential towards E_h. For example, the s particle of the +HCN$(q,s,4)$ model undergoes maximum activation near the resting membrane potential. This leads to maximizing the NSRD, produced by a maximal contribution to the ionic current I_h in cases of hyperpolarization and towards V_{rest} for cases of depolarization. However, the main differential activity between the HCN(r) and HCN(q,s) channels is the quick q particle remaining partially open for all explored values of c. In terms of the negatively shifted model variants, this provides a higher baseline NSRD for the +HCN(q,s) compared to the +HCN(r) model variants.

The relatively short adaptation time constants (τ_{adapt}) of the HH and +KLT models seen in Figure 8c can be clearly interpreted from the PSTHs of those models in Figure 7 that show a sharp decrease in the spike rate following the onset response for stimulation rates above 200 pulses/s. In the same manner, compared to the weakly adapting models, the strongly adapting models clearly boast larger adaptation time constants, which are in the range of 8.5–11 ms. In summary, the shifted $V_{1/2}$ HCN value appears to be the main modulator of the adaptation time constant.

The next portions of Figure 8 plot the NSRD against the onset response rate. Simulation results were provided over all model variants and FEs where Figure 8d–f correspond to the respective stimulation rates: 200, 800, and 5000 pulses/s. The remaining panels, namely Figure 8g–i show experimental data from feline SGN (Zhang et al. 2007) that responded to 250, 1000, and 5000 pulses/s pulse train stimulation. The proportion of strong adapters increases with the pulse rate for both simulation results from this study and those of Zhang et al. (2007). The fact that the NSRD is dependent on pulse rate indicates that accommodation is largely responsible for the occurrence of strongly adapting neurons. The reasoning is that spike rate adaptation should only be dependent on the onset spike rate, not the spike rate decrement, nor the pulse rate. Therefore, if spike rate adaptation were the only contribution to the spike rate, NSRD would not be a function of pulse rate. If spike rate adaptation were the only process responsible for reducing the response rate, all points in Figure 8d–i would lie on a line with positive slope extending from the bottom-left to the top-right corners, suggesting that an increase in onset response rate produces a proportional decrement in activity. Instead, one observes a negative relationship between NSRD and the onset response rate grows stronger with increasing pulse rate, further suggesting that accommodation is at play. It is also worth noting a small discrepancy in NSRD between model simulations in response to a 200 pulses/s stimulation (Fig. 8d) and data from experiment in response to a 250 pulses/s pulse train (Fig. 8i). Specifically, a subset of fibers in the data appears to be strong adapters, whereas the model simulations do not produce strong adapters at this low pulse rate. The strong adapters appear to be independent of the onset response rate, shown in Figure 8i and to a lesser extent in Figure 8h, suggesting that the response of this small subset of neurons may have been subject to fluctuations in excitability in addition to those that are present in models from this study.

Recovery from Masker Train

As seen in Figures 5 and 7, spike rates eventually adapt to a constant steady-state in response to a fixed stimulation rate and current level. Figure 9 shows data from Miller et al. (2011) where low-rate probe train responses of feline SGNs undergo an initial period of reduced excitability after stimulation from either suprathreshold (Fig. 9a, b) or subthreshold (Fig. 9d) high-rate masker trains. Likewise, this study investigated how the masker response history that was driven by a high-rate pulse train contributed to the dynamics of the low-rate probe response. Figure 10 shows the masker and probe response to pulse trains for the same set of model variants as in Figure 7, but for the (a) 1 %, (b) 50 %, (c) 99.99 %, and (d) 99.9999 % FEs at the 5000 pulses/s masker pulse train rate.

Given that the current level was set to a FE = 50 % (or the single-pulse threshold) in the probe-alone condition (i.e., when there was no masker train), a constant response rate was expected similarly to the results of Miller et al. (2011), represented by the gray bars in Figure 9. This would equate to approximately 500 spikes/s within a 1-ms time bin in response to each pulse in the probe train. Over the entire stimulus duration, this produces an average response

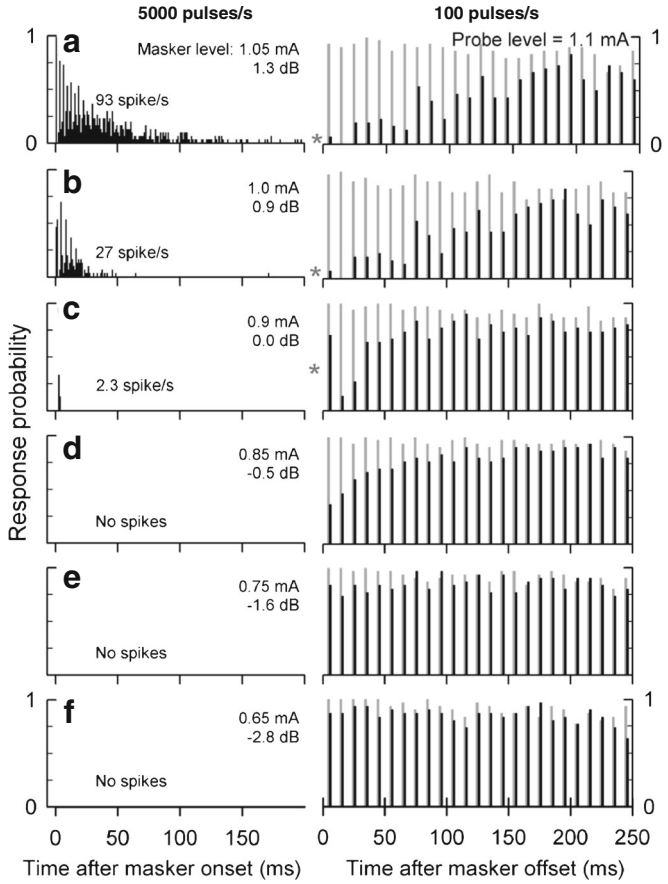

FIG. 9. Feline SGN masker-probe pulse train responses in terms of response probability (= normalized response rate assuming a maximum of one spike per pulse). Masker train responses are shown in the *left subpanels* and the following probe train responses are shown in the companion *right subpanels*. This figure shows cases with masker followed by probe train responses (*black bars*) and probe train alone responses (*gray bars*). All probe train responses are shown with *thicker bars* for visual aid only and were calculated over 1-ms intervals. All masker trains were delivered at rate of 5000 pulses/s over a 200-ms interval. Every probe train was delivered at 100 pulses/s for 250 ms with a pulse current level approximately equivalent to the SPT. **a**–**f** Going from *top* to *bottom* portray responses to decreasing masker pulse levels (shown). *Asterisks* correspond to cases when the first probe response was greater than the second. All panels were adapted with kind permission of Springer Science and Business Media: Figure 1 from Miller et al. (2011), © 2011.

rate of 50 spikes/s. Figure 10 (thick, lightly colored bars) shows that this was indeed the case and was largely independent of the model. The reasons for this behavior can be summarized by the following points: (1) there was no masker stimulus that could pre-condition the probe response and (2) the probe train IPI had a relatively large value of 10 ms (minimizing probe train pulse interactions). The exception to this constant response rate was for the +HCN(r,3), +HCN(q,s,4), and to a lesser extent, the +HCN(r,3) +KLT, +HCN(q,s,4) +KLT models where the probe-alone response displayed adaptation.

In contrast to the probe-alone response, in the masker-probe condition, a flat probe train response due to the pre-conditioning imposed by the masker train on the membrane potential was not expected. Figure 10 superimposes the results of the masker-probe train response (thin dark bars, followed by thick dark bars) over the probe-alone response. Each model's gross probe recovery pattern in the masker-probe condition was such that a gradual increase in the response was observed. This pattern was consistent for masker train pulse current levels that were either greater or less than θ_{SP}, similarly to the experimental results reported by Miller et al. (2011). The only difference between the masker-probe and probe-alone conditions for models HH and +KLT were the weak first probe pulse responses. However, all +HCN model variants shown in Figure 10, namely, +HCN(r,3), +HCN(q,s,4), +HCN(r,3) + KLT, and +HCN(q,s,4) + KLT displayed a longer probe recovery time course than the HH and +KLT models. In particular, model variants +HCN(q,s,4) and +HCN(q,s,4) + KLT had the slowest masker-probe recovery.

Simulation results in Figure 11 show the effect of the HCN $V_{1/2}$ shift (c) on the probe response recovery

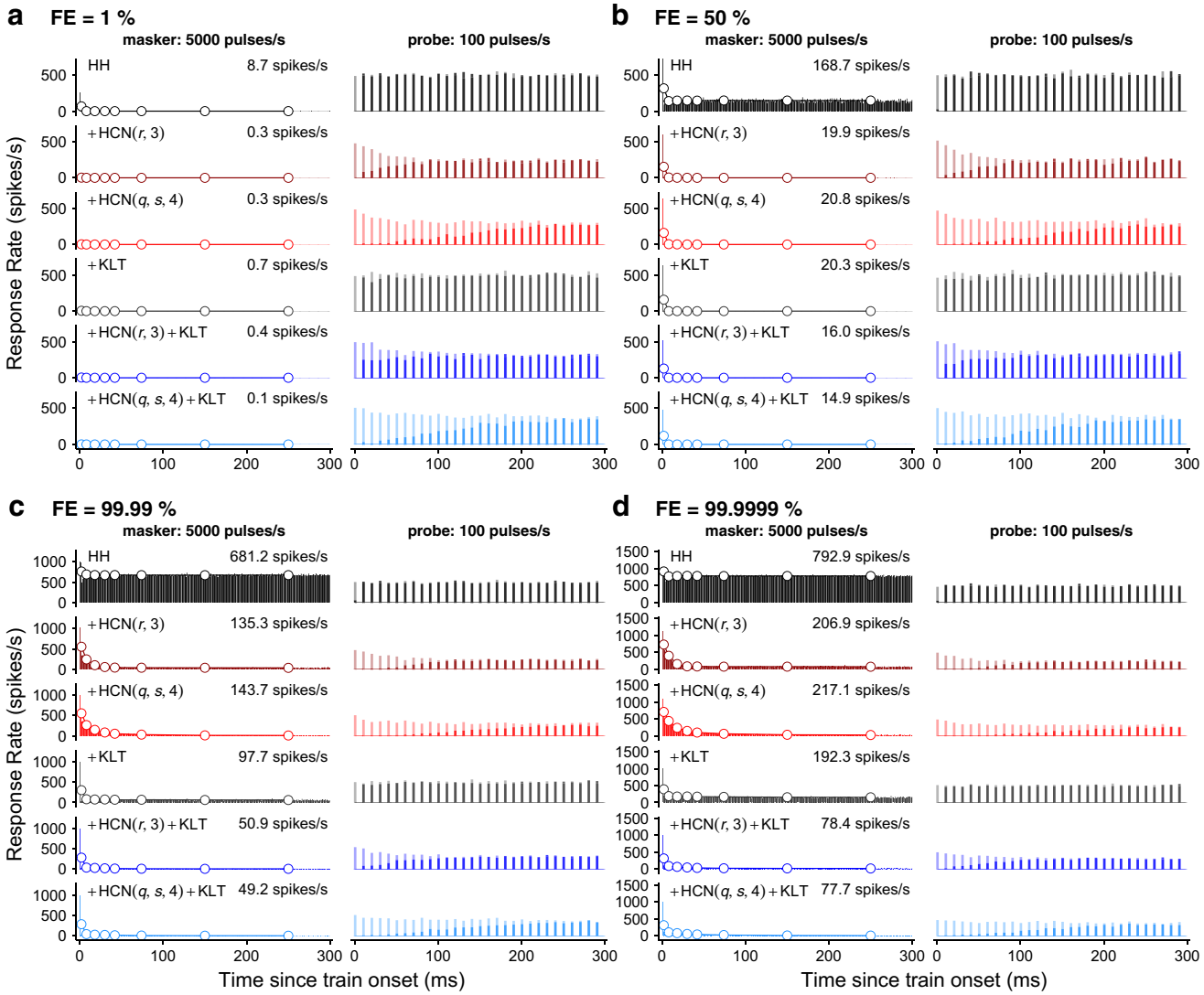

FIG. 10. PSTH or response rate for the strongest-adapting SGN membrane models simulated over a 300-ms interval in response to a 5000 pulses/s masker train followed immediately by a 100 pulses/s probe train. *Dark-colored bars* represent responses to the condition with a masker train (masker-probe), whereas *lighter-colored bars* indicate that no masker train stimulated the neuron (probe-alone). *Panels* represent masker train responses to different FEs: **a** 1 %, **b** 50 %, **c** 99.99 %, and **d** 99.9999 %. All *bars* represent the response rate over 1-ms intervals and *dots* show the response rate over wider intervals (Zhang et al. 2007). Note that the *thicker bars* shown in the probe response panels are for visual aid only and were calculated over 1-ms intervals. The spike rates reported in each masker subpanel were calculated over the 0–300 ms interval.

ratio (PRRR). Figure 11 also shows the PRRR versus the mean response rate to the masker for simulation results (Figure 11b, c) and experimental results (Fig. 11d, e) from Miller et al. (2011). Similarly to the results in Fig. 8a–c, the PRRR shown in Fig. 11a has also been averaged over all FEs (1, 10, 20, 50, 80, 99, 99.99, and 99.9999 %) and the 200, 800, 2000, and 5000 pulses/s stimulation rates. As shown in Fig. 11, the PRRR appears to decrease as a function of the HCN $V_{1/2}$. Comparing this finding to the one in Fig. 8b, this translates to strongly adapting neurons exhibiting a relatively low PRRR, given their differing activation characteristics relative to the weakly adapting HCN variants, which show near complete recovery in their probe response. Figure 11 shows that the negatively shifted HCN model variants have a similarly large PRRR to the HH model of just under 1. Overall, the +HCN model variants show a relatively large PRRR range, with model variants containing the HCN(q,s) channel having the largest range, specifically +HCN($q,s,4$) achieving an average PRRR of less than 0.7.

The channel mechanisms that can explain the change in NSRD as a function of c, may also be used to understand the occurrence of values of PRRR near 1 at smaller values of c. That is, that HCN will not contribute to the total membrane conductance with such $V_{1/2}$ shifts (see Fig. 1). Therefore, the r and s

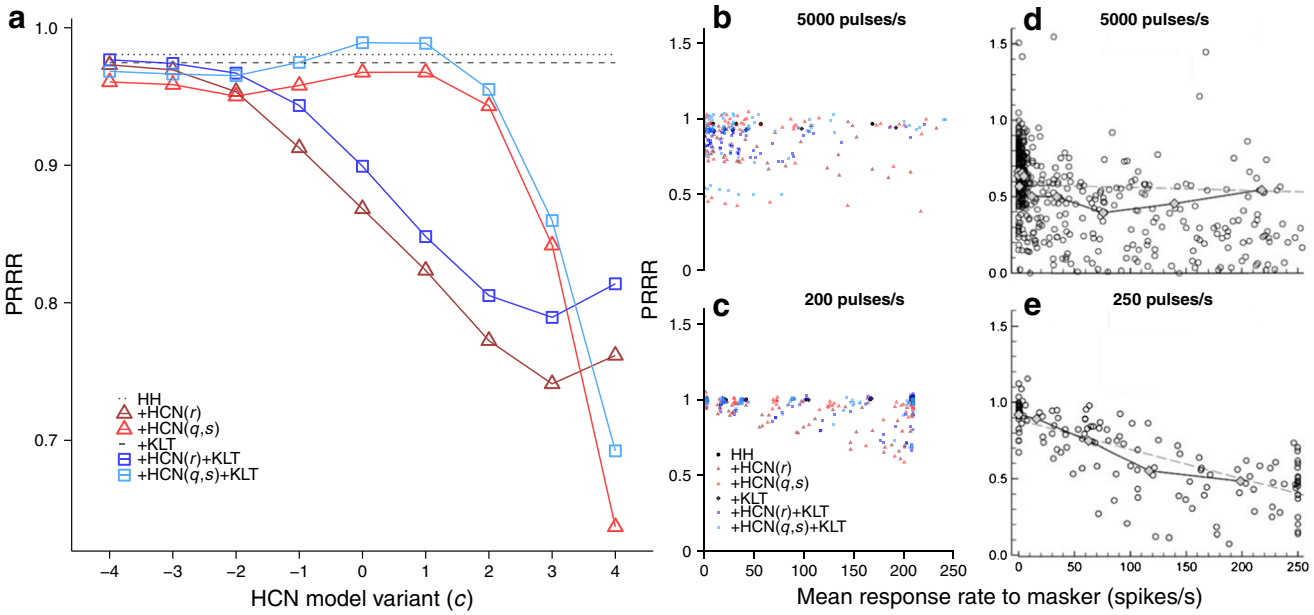

FIG. 11. Summary of the probe response recovery ratio (PRRR). SGN model simulation results show the effect of **a** the HCN $V_{1/2}$ shift parameter c on the PRRR. Visualization of the models follow the conventions introduced in Figure 8. Simulation results (**a**) were averaged over all FEs (1, 10, 20, 50, 80, 99, 99.99, and 99.9999 %) and the 200, 800, 2000, and 5000 pulses/s rates. SGN model simulation results for PRRR as a function of the mean response rate to the masker for the masker pulse train rates of **b** 5000 pulses/s and **c** 200 pulses/s. Here, the mean response rate to the masker was calculated over the entire 0–300 ms masker train interval. **b**, **c** Simulation results across all HCN $V_{1/2}$ levels (−4 to 4) and FEs (1, 10, 20, 50, 80, 99, 99.99, and 99.9999 %). The remaining panels correspond to the same PRRR versus mean response rate to the masker simulation results plot, but for feline SGN recordings responding to **d** 5000 pulses/s and **e** 250 pulses/s masker-probe pulse train stimulation, where the mean response rate to the masker was calculated over the entire 0–200 ms masker train interval. **d**, **e** Adapted with kind permission of Springer Science and Business Media: Figure 3d, e from Miller et al. (2011), © 2011.

channel particles cannot contribute to the afterhyperpolarization phase, nor can they regulate the resting membrane potential. These channel particles are responsible for reducing excitability on the timescale of approximately 100 ms which may partially explain the probe recovery in response to pulse train stimulation at 100 pulses/s, in contrast to the quicker-responding q particle (see τ_q in Fig. 1).

There are similar trends in the PRRR versus the mean response rate to the masker as a function of the pulse rate. That is, whereas the 5000 pulses/s case (Fig. 11b, d) shows a shallow negative slope, the slower pulse rates (Fig. 11c = 200 pulses/s; Fig. 11e = 250 pulses/s) express a steeper one. However, the full range of experimental PRRR values reported from Miller et al. (2011) cannot be matched by the simulation results of this study and therefore cannot be explained. Particularly, the recovery of the response to the 100 pulses/s probe train is poor (low PRRR) in a subset of neurons when preconditioned with a 5000 pulses/s masker train. This phenomena was conserved for the entire range of mean response rates to the masker (see Fig. 11d) whereas the simulation results of any model SGNs could not produce this activity (see Fig. 11c). This behavior may indicate a low absolute PRRR in a subset of neurons. This could correspond to a subset of neurons that were subject to fluctuations in excitability in addition to those that are present in this study's models, such as was the case for Figure 8. Alternatively, given that a probe train interval of 300 ms was used in this study that is somewhat longer than the probe train interval of 250 ms used by Miller et al. (2011), the model SGN may have been capable of more recovery, thus increasing the PRRR.

Refractoriness

Figure 12 shows the threshold recovery data as a function of the IPI for simulation results and those from experimental feline SGN recordings (Miller et al. 2001). Figure 12a presents the threshold recovery ratio for the strongest-adapting model variants. The corresponding parameter estimates have been extracted from the fit to (4) and are given in Table 2. By comparing HH, +HCN$(r,3)$, and +HCN$(q,s,4)$ to +KLT, +HCN$(r,3)$ +KLT, and +HCN$(q,s,4)$ +KLT in Fig. 12, KLT appears to be responsible for increasing the ARP (Δt_{abs}) and the RRP time course. Table 2 lists the values of Δt_{abs} and the larger of the two time constants τ_2 where the effect of KLT appears to be an additive one. In contrast, the presence of KLT reduces τ_1. Nevertheless, the addition

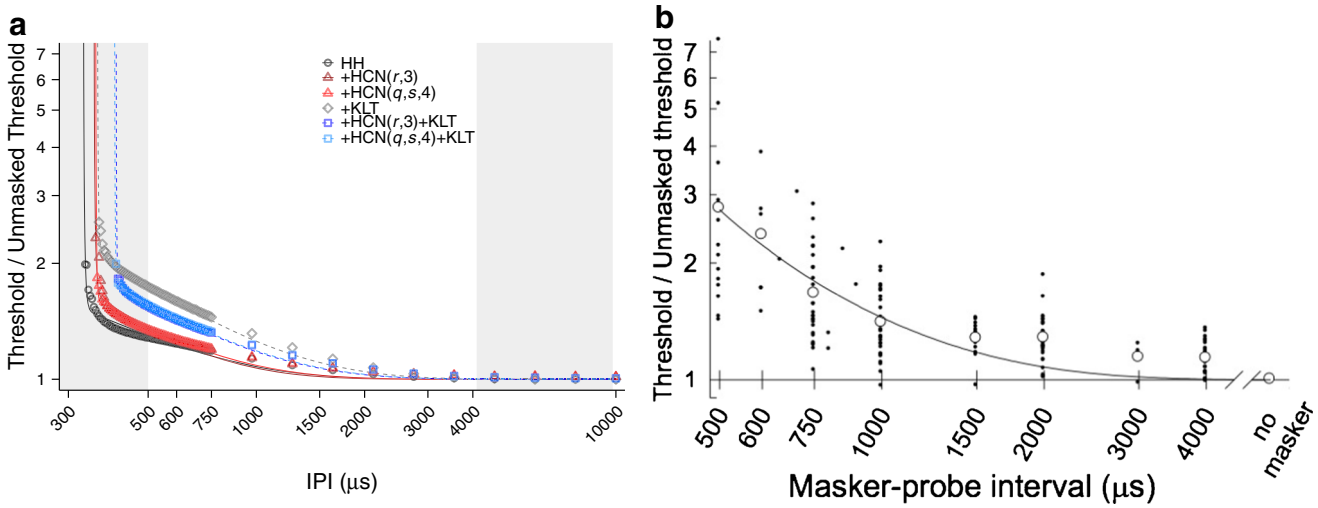

FIG. 12. Refractory threshold ratio as a function of the interval between pulses. **a** Threshold/umasked threshold (θ_{ref}/θ_{SP}) versus interpulse interval (IPI) for the strongest-adapting SGN membrane models. Note that θ_{ref}/θ_{SP} and IPI are scaled on a log-10 axis. **b** Threshold/umasked threshold as a function of the masker-probe interval (or IPI) from feline SGN (Miller et al. 2001). *Grayed areas* (**a**) indicate ranges of the data not shown (**b**). **b** Reprinted with kind permission of Springer Science and Business Media: Figure 6 from Miller et al. (2001), © 2001.

of KLT to any model cannot produce a sufficiently long relative refractory period as observed by Miller et al. (2001) (see Fig. 12b) where the effects of relative refractoriness persist until at least 4 ms in a sizable subset of fibers. Negm and Bruce (2014) reported similar ARP findings. While the ARP values reported in this study are slightly different than those of Negm and Bruce (2014) and Miller et al. (2001), this can be attributed to several factors. One reason could be due to the ability of the spike detection algorithm used in this study to discriminate spikes when the sodium conductance duration is greater than θ_λ even if $V(t)$ is less than an arbitrary spike detection threshold, especially for small IPIs (e.g., response to the second pulse for the refractory simulation). Another reason may be due to stimulus duration-dependent refractoriness, in which stimulation delivered during the absolute refractory period effectively prolongs the absolute refractory period (Morse et al. 2015). Whereas Negm and Bruce (2014) used biphasic pulses with 75-μs duration and 75-μs interphase gap, 50-μs duration monophasic pulses were used in this study in order to be more consistent with the Miller et al. (2001) stimulation paradigm. Finally, unlike the extracellular stimulation used by Miller et al. (2001), this study used a single-node SGN model with "intracellular" stimulation, which would not be subject to conduction block imposed by the absolute refractory period at neighboring nodes of Ranvier. With the exception of the +KLT model, all models shown in Table 2 exhibit a greater effect of the short time constant τ_1 on the RRP ($A_1 > A_2$).

The effect of HCN on the refractory response of the membrane models becomes more apparent in Figure 13 as the ARP is plotted against the HCN $V_{1/2}$ shift c. The Δt_{abs} is approximately constant for values of $c < 0$. However, beyond that, Δt_{abs} increases as a function of c. The additive effect of KLT is invariant for all values of c when comparing +HCN(r) and +HCN(q,s) to +HCN(r) +KLT and +HCN(q,s) +KLT.

DISCUSSION

Woo et al. (2009a,b, 2010) demonstrated spike rate adaptation in model SGNs by incorporating an

TABLE 2

Refractory recovery function parameter estimates for strongest-adapting model variants

Model	A_1	A_2	Δt_{abs}(ms)	τ_1 (μs)	τ_2 (ms)	R^2
HH	2.05	1.05	0.329	4.90	0.46	0.935
+HCN(r,3)	1.81	1.21	0.353	3.41	0.35	0.927
+HCN(q,s,4)	1.94	1.17	0.357	2.10	0.42	0.971
+KLT	1.40	1.64	0.360	2.71	0.64	0.969
+HCN(r,3) + KLT	1.74	1.28	0.407	1.79	0.58	0.991
+HCN(q,s,4) + KLT	1.75	1.31	0.403	1.98	0.60	0.995

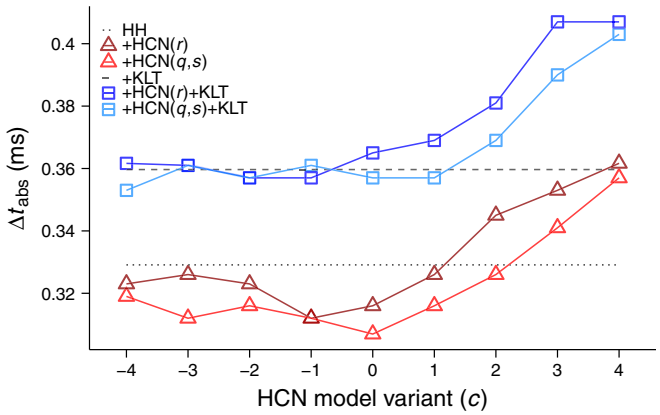

FIG. 13. Absolute refractory period versus the HCN $V_{1/2}$ shift parameter c for each of the membrane models. Visualization of the models follow the conventions introduced in Figure 8

extracellular potassium accumulation phenomenon, native to leech central nervous system (Baylor and Nicholls 1969), into a Hodgkin-Huxley model. Miller et al. (2011) showed that the addition of a KLT channel in concert with the K^+ accumulation mechanism was capable of explaining accommodation (or subthreshold adaptation) in response to pulse train stimulation. They also proposed variation in axonal diameter as a potential factor in determining the degree of SGN adaptation (Woo et al. 2010). However, the relatively large ARP values reported by Miller et al. (2011) were not representative of the ARP values collected experimentally from feline SGNs (Miller et al. 2001). This suggests that alternative mechanisms may be necessary to holistically explain the SGN response to high-rate electrical stimulation.

This study has established that HCN channels may be responsible for strong adaptation in response to pulsatile stimulation through the combination of both spike rate adaptation and the buildup of accommodation that is observed in SGNs. For strongly adapting SGN models, all of which contain HCN channels, this study has shown that the time course over which adaptation acts (8.5–11 ms) qualitatively agrees with the mean rapid adaptation time constant values in feline SGNs (8.2–11.8 ms) (Zhang et al. 2007) across a range of pulse train rates (250, 1000, and 5000 pulses/s). Although a greater number of the +HCN(r) than the +HCN(q,s) model variants exhibit strong adaptation, the +HCN(q,s) model has benefits of (1) having the largest range in PRRR which is similar to the results found by Miller et al. (2011) and (2) the HCN(q,s) channel model is representative of channels found in the SGN (Liu et al. 2014b). Additionally, the +HCN(q,s) model variants display less adaptation to the low-frequency probe-alone pulse train than +HCN(r) model variants (recall Fig. 10).

This study has also ascertained that HCN may contribute towards determining the absolute refractory period in SGNs.

The simulation results of this study are dependent on the configuration of the HCN channel activation characteristics (Chen 1997; Kim and Holt 2013; Liu et al. 2014b; Mo and Davis 1997; Yi et al. 2010). The ranges of explored HCN $V_{1/2}$ values was extended by doubling the ranges estimated by Liu et al. (2014b) in neonatal murinae, i.e., ±4 standard deviations rather than ±2 standard deviations around the mean. This wider range was motivated by the lack of knowledge about the precise range of values for feline SGNs and possible differences in the resting membrane potential of murinae and adult feline SGNs. However, a change of approximately four standard deviations in HCN $V_{1/2}$ was sufficient to almost completely account for the variability in degree of spike rate adaptation, accommodation, and refractoriness observed in response to CI stimulation (see Figs. 8b and 11a). For the older HCN(r) model, the range of values over which the model changed from being non-adapting to strongly adapting was centered around the mean HCN $V_{1/2}$, i.e., for shift values of c between approximately −2 and +2. For the newer HCN(q,s) channel model, the effective range for c to modulate the strength of adaptation was between +1 and +4, suggesting that the mean HCN $V_{1/2}$ for adult feline SGNs may be at more positive values than was estimated for neonatal murinae by Liu et al. (2014b). It has been noted by Davis and Crozier (2015) that adult SGNs have the capability to regulate their strength of adaptation, so the difference in the range of effective $V_{1/2}$ in the +HCN(q,s) model of adult feline SGNs compared to the range measured by Liu et al. (2014b) may be due to both species and age differences. Shifting the value of $V_{1/2}$ of a channel model changes the operating range as a function of

the membrane potential of that channel (Krouchev et al. 2015). This can amount to a voltage-dependent "thresholding" effect on the channel's activity and as such, was deemed an appropriate HCN model parameter to vary as a first step towards explaining the variability of SGN excitability. Other channel parameters can play a role in regulating channel activity other than $V_{1/2}$ such as the slope factor, reversal potential, activation minimum, and activation maximum. These values may be explored in future studies to further fine-tune the SGN response, given supporting experimental evidence of the variation in these parameters.

Together with the refractory behavior reported by Negm and Bruce (2014), the results of this study have shown that KLT can increase the ARP and RRP time constants within physiological bounds, compared to the HH model. However, despite the qualitative increase in the RRP time constant, the models cannot predict the extended relative refractoriness observed in a subset of SGNs, as previously reported (Botros and Psarros 2010; Cartee et al. 2000; Cohen 2009; Miller et al. 2001). The same Na_v and K_v ion channels used in the alternative model of Woo et al. (Miller et al. 2011; Woo et al. 2009a,b, 2010) were kept in order to directly compare the results of this study with theirs, the only difference being in the adaptation mechanisms. However, the model's AP duration is somewhat shorter than the value of 330 μs recently estimated for adult SGNs (Rattay and Danner 2014). This possible inaccuracy, along with the discrepancy in refractory properties for some SGNs, suggests that further refinement of the types and characteristics of ion channels included in SGN models is warranted. A number of different Na_v and K_v channel descriptions have been explored in previous SGN models (see O'Brien and Rubinstein 2016, for a recent review), but none of these models have incorporated HCN channels. The emerging extended relative refractoriness shown in models with KLT is motivation for experimentally determining the channel's kinetics and the possible nodal and juxtaparanodal distribution (Lai and Jan 2006; Rasband and Shrager 2000) that are specific to feline SGN. Exploring different channel types and configurations found in SGNs such as different Na_v, high-threshold K, and other K channels (recall Davis and Crozier 2015) should be a step in a positive direction, as this study has shown that more accurate characterizations of HCN channels endogenous to SGNs can better explain in vivo responses to CI stimulation on the order of 10 to 100 ms. These different channels may shed light on the differences in action potential duration and refractoriness, as well as the very slow (>1 s) adaptation observed in some SGNs (Litvak et al. 2003). However, as demonstrated in this study, there is a significant scope for heterogeneity of channel properties alone to account for variability in stimulus-response statistics.

CONCLUSION

This study has shown that heterogeneity in the half-maximal activation potential of HCN channels can explain the variability of adaptation in SGNs responding to pulsatile CI stimulation while maintaining a physiologically realistic absolute refractory period. A better understanding of the mechanisms behind intrinsic adaptation of SGNs is important for determining how different SGNs in the auditory nerve might respond differently to the same electrical stimulus. In addition, the degree of adaptation may also vary with the site of action potential initiation, because of differential expression of ion channel types at different locations along the neuron. Finally, a more accurate computational model of SGNs that can incorporate the range of adaptation strengths observed *in vivo* should provide an invaluable tool for evaluating CI stimulating strategies in present clinical use, as well as for the development of novel stimulation approaches.

ACKNOWLEDGEMENTS

The authors would like to thank Dr. Paul Manis for supplying his HCN(q,s) channel model code and Dr. Paul Abbas for permitting use of previously published figures. The feedback of the anonymous reviewers on earlier versions of the manuscript was also extremely helpful. This work was supported by NSERC Discovery Grant 261736 (ICB).

COMPLIANCE WITH ETHICAL STANDARDS

Conflict of Interest The authors declare no conflicts of interest in any form.

APPENDIX

For the equations that model the current and channel kinetics of the Na_v, K_v, and KLT channels, please refer to the Appendix in Negm and Bruce (2014). Here are the equations describing the voltage-gated activity of the HCN(r) and HCN(q,s) channel models are supplied, shifted by $cV_{1/2}$ standard deviations as functions of the relative membrane potential (σ_x, where x is the channel particle; refer to Table 1 for individual values).

HCN(r) channel model:

The ionic current follows

$$I_{\mathrm{h},r}(t) = \gamma_{\mathrm{h}} N_{r1}(t)\left[V_{\mathrm{m}}(t) - E_{\mathrm{h},r}\right] \tag{6}$$

where γ_{h} is the single-channel conductance, $E_{\mathrm{h},r}$ is the reversal potential, $V_{\mathrm{m}}(t)$ is the membrane potential at time t, and $N_{r_1}(t)$ is the number of channels in the fully open, conducting state governed by the kinetic Markov chain state transition diagram

$$r_0 \underset{\beta_r}{\overset{\alpha_r}{\rightleftharpoons}} r_1 \tag{7}$$

where transition rates α_r and β_r, calculated by (19) and (20), are dependent on the relative membrane potential (V) and are functions of the activation function (r_∞) and time constant (τ_r) below

$$r_\infty(V) = \frac{1}{1 + 5.879\exp[(V - c\sigma_r)/7]} \tag{8}$$

$$\tau_r(V) = 4.17 + \frac{758.8\exp[(V - c\sigma_r)/14]}{1 + 9.199\exp[13(V - c\sigma_r)/84]} \tag{9}$$

where c extends from −4 to 4.

HCN(q, s) channel model:

The ionic current follows

$$I_{\mathrm{h},(q,s)}(t) = \gamma_{\mathrm{h}}\left[N_{q_2}(t) + N_{s_1}(t)\right]\left[V_{\mathrm{m}}(t) - E_{\mathrm{h},(q,s)}\right] \tag{10}$$

where $N_{q_2}(t)$ and $N_{s_1}(t)$ are the number of channels in the fully open, conducting states governed by the parallel kinetic Markov chain state transition diagram

$$\begin{array}{l} q_0 \underset{\beta_q}{\overset{2\alpha_q}{\rightleftharpoons}} q_1 \underset{2\beta_q}{\overset{\alpha_q}{\rightleftharpoons}} q_2 \\ s_0 \underset{\beta_s}{\overset{\alpha_s}{\rightleftharpoons}} s_1 \end{array} \tag{11}$$

where transition rates α_q, β_q, α_s, and β_s, calculated by (19) and (20), are dependent on the relative membrane potential and are functions of the activation functions (q_∞, s_∞) and time constants (τ_q, τ_s) below

$$q_\infty(V) = \frac{1}{\left(1 + 9.104\exp\left[(V - c\sigma_q)/12.36\right]\right)^{1/2}} \tag{12}$$

$$s_{A,\infty}(V) = \frac{0.6628}{1 + 17.09\exp[(V - c\sigma_s)/4.883]} \tag{13}$$

$$s_{B,\infty}(V) = \frac{1 - 0.6628}{1 + 3648\exp[(V - c\sigma_s)/3.927]} \tag{14}$$

$$s_\infty(V) = \frac{s_{A,\infty}(V) - s_{B,\infty}(V)}{0.5551729} \tag{15}$$

$$\tau_q(V) = \frac{60.98\exp\left[(V - c\sigma_q)/21.48\right]}{1 + 2.107\exp\left[(V - c\sigma_q)/12.19\right]} \tag{16}$$

$$\tau_s(V) = \frac{632.3\exp[(V - c\sigma_s)/20.23]}{1 + 7.925\exp[(V - c\sigma_s)/13.44]}. \tag{17}$$

Neuron-specific channel modifications

The original channel time constants for KLT: τ_w and τ_z (Rothman and Manis 2003a) and HCN: τ_r (Rothman and Manis 2003b); τ_q and τ_s (Liu et al. 2014b) were divided by their respective thermal scaling coefficients k_w, k_z, k_r, k_q, and k_s to adjust the temperature to 37 °C where

$$k_x = Q_{10,x}^{(T - T_0)/10} \tag{18}$$

and x is the channel particle and $Q_{10,x}$ (see Table 1 for channel-specific values) represents the rate gain for two temperature-dependent biological processes separated by 10 °C (Cartee 2000). T_0 represents the original temperature whereas T is the current temperature. The transition rates were then computed as

$$\alpha_x(V) = x_\infty(V)/\tau_x(V) \tag{19}$$

$$\beta_x(V) = [1 - x_\infty(V)]/\tau_x(V) \tag{20}$$

with the steady-state activation functions (x_∞) and time constants (τ_x).

REFERENCES

Arora K, Dawson P, Dowell R, Vandali A (2009) Electrical stimulation rate effects on speech perception in cochlear implants. Int J Audiol 48(8):561–567

Baylor DA, Nicholls JG (1969) Changes in extracellular potassium concentration produced by neuronal activity in the central nervous system of the leech. J Physiol 203(3):555–569

Benarroch EE (2013) HCN channels: function and clinical implications. Neurology 80(3):304–310

Biel M, Wahl-Schott C, Michalakis S, Zong X (2009) Hyperpolarization-activated cation channels: from genes to function. Physiol Rev 89(3):847–885

Botros A, Psarros C (2010) Neural response telemetry reconsidered: II. The influence of neural population on the ECAP recovery function and refractoriness. Ear Hear 31(3):380–391

Boulet J, White MW, Bruce IC (2016) Temporal considerations for stimulating spiral ganglion neurons with cochlear implants. J Assoc Res Otolaryngol 17(1):1–17

Bruce IC (2006) Implementation issues in approximate methods for stochastic Hodgkin-Huxley models. Ann Biomed Eng 35(2):315–318

Bruce IC, White MW, Irlicht LS, O'Leary SJ, Clark GM (1999a) The effects of stochastic neural activity in a model predicting intensity perception with cochlear implants: low-rate stimulation. IEEE T Bio-Med Eng 46(12):1393–1404

Bruce IC, White MW, Irlicht LS, O'Leary SJ, Dynes S, Javel E, Clark GM (1999b) A stochastic model of the electrically stimulated auditory nerve: single-pulse response. IEEE T Bio-Med Eng 46(6):617–629

Cao XJ, Oertel D (2011) The magnitudes of hyperpolarization-activated and low-voltage-activated potassium currents co-vary in neurons of the ventral cochlear nucleus. J Neurophysiol 106(2):630–640

Cartee LA (2000) Evaluation of a model of the cochlear neural membrane. II: comparison of model and physiological measures of membrane properties measured in response to intrameatal electrical stimulation. Hear Res 146(1–2):153–166

Cartee LA, van den Honert C, Finley CC, Miller RL (2000) Evaluation of a model of the cochlear neural membrane. I. Physiological measurement of membrane characteristics in response to intrameatal electrical stimulation. Hear Res 146(1–2):143–152

Cartee LA, Miller CA, van den Honert C (2006) Spiral ganglion cell site of excitation I: comparison of scala tympani and intrameatal electrode responses. Hear Res 215(1–2):10–21

Chen C (1997) Hyperpolarization-activated current (I_h) in primary auditory neurons. Hear Res 110(1–2):179–190

Cohen LT (2009) Practical model description of peripheral neural excitation in cochlear implant recipients: 5. Refractory recovery and facilitation. Hear Res 248(1–2):1–14

Davis RL, Crozier RA (2015) Dynamic firing properties of type I spiral ganglion neurons. Cell Tissue Res 361(1):115–127

Dynes SBC (1996) Discharge characteristics of auditory nerve fibers for pulsatile electrical stimuli. PhD thesis, Massachusetts Institute of Technology, Cambridge, Massachusetts

Gillespie DT (1977) Exact stochastic simulation of coupled chemical reactions. J Phys Chem 81(25):2340–2361

Guevara MR (2003) Bifurcations involving fixed points and limit cycles in biological systems. In: Beuter A, Glass L, Mackey MC, Titcombe MS (eds) Nonlinear dynamics in physiology and medicine. Springer New York, New York, NY, pp. 41–85

Heffer LF, Sly DJ, Fallon JB, White MW, Shepherd RK, O'Leary SJ (2010) Examining the auditory nerve fiber response to high rate cochlear implant stimulation: chronic sensorineural hearing loss and facilitation. J Neurophysiol 104(6):3124–3135

Hodgkin AL, Huxley AF (1952) A quantitative description of membrane current and its application to conduction and excitation in nerve. J Physiol 117(4):500–544

Howells J, Trevillion L, Bostock H, Burke D (2012) The voltage dependence of I_h in human myelinated axons. J Physiol Lond 590(Pt 7):1625–1640

Hugenard JR, McCormick DA (1992) Simulation of the currents involved in rhythmic oscillations in thalamic relay neurons. J Neurophysiol 68(4):1373–1383

Imennov NS, Rubinstein JT (2009) Stochastic population model for electrical stimulation of the auditory nerve. IEEE T Bio-Med Eng 56(10):2493–2501

Jenks GF (1967) The data model concept in statistical mapping. In: Frenzel K (ed) International yearbook of cartography, George Philip & Son, pp 186–190

Kim YH, Holt JR (2013) Functional contributions of HCN channels in the primary auditory neurons of the mouse inner ear. J Gen Physiol 142(3):207–223

Krouchev NI, Rattay F, Sawan M, Vinet A (2015) From squid to mammals with the HH model through the Na_v channels' half-activation-voltage parameter. PLoS One 10(12):e0143,570–e0143,531

Lai HC, Jan LY (2006) The distribution and targeting of neuronal voltage-gated ion channels. Nat Rev Neu-rosci 7(7):548–562

Litvak LM, Smith ZM, Delgutte B, Eddington DK (2003) Desynchronization of electrically evoked auditory-nerve activity by high-frequency pulse trains of long duration. J Acoust Soc Am 114(4 Pt 1):2066–2078

Liu Q, Lee E, Davis RL (2014a) Heterogeneous intrinsic excitability of murine spiral ganglion neurons is determined by Kv1 and HCN channels. Neuroscience 257:96–110

Liu Q, Manis PB, Davis RL (2014b) I_h and HCN channels in murine spiral ganglion neurons: tonotopic variation, local heterogeneity, and kinetic model. J Assoc Res Otolaryngol 15(4):585–599

Long JS (1997) Regression models for categorical and limited dependent variables. Advanced quantitative techniques in the social sciences. SAGE Publications Inc, Thousand Oaks, CA

Miller C, Abbas PJ, Nourski KV, Hu N, Robinson BK (2003) Electrode configuration influences action potential initiation site and ensemble stochastic response properties. Hear Res 175(1–2):200–214

Miller CA, Abbas PJ, Robinson B (2001) Response properties of the refractory auditory nerve fiber. J Assoc Res Otolaryngol 2(3):216–232

Miller CA, Hu N, Zhang F, Robinson BK, Abbas PJ (2008) Changes across time in the temporal responses of auditory nerve fibers stimulated by electric pulse trains. J Assoc Res Otolaryngol 9(1):122–137

Miller CA, Woo J, Abbas PJ, Hu N, Robinson BK (2011) Neural masking by sub-threshold electric stimuli: animal and computer model results. J Assoc Res Otolaryngol 12(2):219–232

Mino H, Rubinstein JT, White JA (2002) Comparison of algorithms for the simulation of action potentials with stochastic sodium channels. Ann Biomed Eng 30(4):578–587

Mino H, Rubinstein JT, Miller CA, Abbas PJ (2004) Effects of electrode-to-fiber distance on temporal neural response with electrical stimulation. IEEE Trans Biomed Eng 51(1):13–20

Mo ZL, Davis RL (1997) Heterogeneous voltage dependence of inward rectifier currents in spiral ganglion neurons. J Neurophysiol 78(6):3019–3027

Morse RP, Allingham D, Stocks NG (2015) Stimulus-dependent refractoriness in the Frankenhaeuser-Huxley model. J Theo Biol 382(C):397–404

Negm MH, Bruce IC (2008) Effects of I_h and I_{KLT} on the response of the auditory nerve to electrical stimulation in a stochastic Hodgkin-Huxley model. Proc 30th Annu Int Conf IEEE Eng Med Biol Soc 2008:5539–5542

NEGM MH, BRUCE IC (2014) The effects of HCN and KLT ion channels on adaptation and refractoriness in a stochastic auditory nerve model. IEEE T Bio-Med Eng 61(11):2749–2759

O'BRIEN GE, RUBINSTEIN JT (2016) The development of biophysical models of the electrically stimulated auditory nerve: Single-node and cable models. Network pp 1–22

RASBAND MN, SHRAGER P (2000) Ion channel sequestration in central nervous system axons. J Physiol 525(Pt1):63–73

RATTAY F, DANNER SM (2014) Peak I of the human auditory brainstem response results from the somatic regions of type I spiral ganglion cells: evidence from computer modeling. Hear Res 315:67–79

ROBINSON RB, SIEGELBAUM SA (2003) Hyperpolarization-activated cation currents: from molecules to physiological function. Annu Rev Physiol 65:453–480

ROTHMAN JS, MANIS PB (2003A) Kinetic analyses of three distinct potassium conductances in ventral cochlear nucleus neurons. J Neurophysiol 89(6):3083–3096

ROTHMAN JS, MANIS PB (2003B) The roles potassium currents play in regulating the electrical activity of ventral cochlear nucleus neurons. J Neurophysiol 89(6):3097–3113

RUBINSTEIN JT (1995) Threshold fluctuations in an N sodium channel model of the node of Ranvier. Biophys J 68(3):779–785

RUSZNÁK Z, SZŰCS G (2008) Spiral ganglion neurones: an overview of morphology, firing behaviour, ionic channels and function. Pflugers Arch - Eur J Physiol 457(6):1303–1325

SCHNEIDMAN E, FREEDMAN B, SEGEV I (1998) Ion channel stochasticity may be critical in determining the reliability and precision of spike timing. Neural Comput 10(7):1679–1703

VERVEEN AA (1962) Axon diameter and fluctuation in excitability. Acta Morphol Neerl Scand 5:79–85

VERVEEN AA, DERKSEN HE (1968) Fluctuation phenomena in nerve membrane. Proc IEEE 56(6):906–916

WOO J, MILLER CA, ABBAS PJ (2009A) Biophysical model of an auditory nerve fiber with a novel adaptation component. IEEE T Bio-Med Eng 56(9):2177–2180

WOO J, MILLER CA, ABBAS PJ (2009B) Simulation of the electrically stimulated cochlear neuron: modeling adaptation to trains of electric pulses. IEEE T Bio-Med Eng 56(5):1348–1359

WOO J, MILLER CA, ABBAS PJ (2010) The dependence of auditory nerve rate adaptation on electric stimulus parameters, electrode position, and fiber diameter: a computer model study. J Assoc Res Otolaryngol 11(2):283–296

YI E, ROUX I, GLOWATZKI E (2010) Dendritic HCN channels shape excitatory postsynaptic potentials at the inner hair cell afferent synapse in the mammalian cochlea. J Neurophysiol 103(5):2532–2543

ZHANG F, MILLER CA, ROBINSON BK, ABBAS PJ, HU N (2007) Changes across time in spike rate and spike amplitude of auditory nerve fibers stimulated by electric pulse trains. J Assoc Res Otolaryngol 8(3):356–849